Practical Waveform-to-Energy Harvesting Model and Transmit Waveform Optimization for RF Wireless Power Transfer Systems

Nachiket Ayir, *Member, IEEE*, Taneli Riihonen, *Senior Member, IEEE*, and Mikko Heino, *Member, IEEE*

***Abstract*— The received radio-frequency (RF) power in far-field RF wireless power transfer (WPT)—with or without simultaneous information transfer—is minuscule due to large propagation loss in wireless media. In such scenarios, adapting to the receiver characteristics by transmit waveform optimization is essential for maximizing the harvested direct current (dc) and, thus, the end-to-end efficiency of an RF WPT system. The receiver efficiency in RF WPT is governed by the RF-to-dc efficiency of the rectifier as well as the impedance mismatch at the antenna and load. In this article, we study the receiver efficiency for any fixed load and, subsequently, present a novel rectifier model that relates the average harvested dc power to the distribution, that is, the histogram, of the instantaneous power levels of the RF signal's envelope over time. The proposed waveform-to-energy harvesting (EH) model enables us to anticipate the average harvested dc power for any waveform, including communication signals as well, given the knowledge of the power-level distribution. Consequently, we conduct rigorous waveform optimization to maximize the average harvested dc power and determine the digital baseband signal at the transmitter that does so, namely prove that a pulsed tone at appropriate frequency is optimal for RF WPT. We present a multiband test-bed for determining the receiver efficiency for any digital baseband waveform. The efficacy of the proposed model is corroborated through experiments as well as simulations, which confirm that it is operational as well as accurate in practice and that single-sine pulses yield higher efficiency than basic multisine waveforms, while a pulsed phase shift keying (PSK) is preferable for simultaneous wireless information and power transfer (SWIPT).**

***Index Terms*— Multiband test-bed, rectifier model, simultaneous wireless information and power transfer (SWIPT), waveform optimization, wireless power transfer (WPT).**

I. Introduction

FAR-FIELD radio-frequency (RF) wireless power transfer (WPT) and simultaneous wireless information and power transfer (SWIPT) are eminent research topics [1], [2] with potential applications in consumer and industrial Internet-of-Things (IoT). RF WPT alone could provide the multitude of IoT sensors with a replenishable energy source, thus averting sensors from becoming hazardous environmental waste after their batteries die and also avoiding the hassle of replacing the batteries given the sheer size of an IoT network. An RF WPT-enabled sensor would comprise a rectenna (a portmanteau for the combination of a receiver antenna and an RF diode-based rectifier) to convert the incident RF energy to direct current (dc) energy, and possibly store it temporarily in its supercapacitor. While an RF WPT transmitter usually operates in a single band, the sensors should practically be able to harvest energy from multiple such RF bands to maximize their dc output.

While the focus of RF WPT is to energize the receiver sensors through RF radiation, the spectrum could be leveraged better by utilizing it to transport information as well as power together, thus giving rise to the concept of RF SWIPT. The energy and information receivers could either be colocated or separate depending on the application and device complexity. RF SWIPT can also leverage the networking paradigms of wireless-powered communication and backscatter networking, where energy is transferred in the downlink and the transceiver spends it to transmit information in the uplink [1].

A. Motivation

The state-of-the-art WPT technologies enable energy transfer over short-range (about an inch), mid-range (about 1–2 m), and far-field. All these competing technologies have their own benefits and limitations [3], [4], [5], [6]. Moreover, each of the three technologies has commercially available products. While far-field RF WPT that is in the scope of this work provides the benefits of mobility and longer operation range over the other two, it comes with additional complexities too.

Especially, RF WPT suffers from immense over-the-air propagation losses resulting in only a small fraction of the actual transmitted power reaching the receiver. This necessitates optimizing receiver performance in RF WPT systems to reduce the disadvantage. Consequently, a majority of the research on RF WPT systems has thus far focused on technical problems associated with the energy harvesting (EH) receiver [7]. The performance of the receiver in RF WPT is characterized by its efficiency, which is the ratio of the average harvested dc power ($P_{\text{out}}^{\text{dc}}$) to the average RF input power ($P_{\text{in}}^{\text{RF}}$).

The receiver in RF WPT generally comprises a receiving antenna, a matching network, a rectifier, and a load. To optimize the receiver performance in RF WPT, it is

Manuscript received 24 January 2023; revised 6 April 2023; accepted 16 May 2023. This work was supported in part by the Finnish Cultural Foundation Grant and in part by the Academy of Finland under Grant 341489/346622. *(Corresponding author: Nachiket Ayir.)*

The authors are with the Faculty of Information Technology and Communication Sciences, Tampere University, 33720 Tampere, Finland (e-mail: nachiket.ayir@tuni.fi; taneli.riihonen@tuni.fi; mikko.heino@tuni.fi).

Color versions of one or more figures in this article are available at https://doi.org/10.1109/TMTT.2023.3284261.

Digital Object Identifier 10.1109/TMTT.2023.3284261

first essential to have an accurate mathematical model of an RF energy harvester. It is already well established in the existing literature [7] that linear EH models cannot capture the true behavior of a diode-based rectifier, while nonlinear EH models can characterize the rectifier behavior in different power regimes [8]. In this article, we present a novel nonlinear rectifier model that relies on the characteristics of the input waveform. We review the existing nonlinear EH models in Section I-B for reference.

B. Literature Review

While the practical applications of RF WPT are slowly on the rise, there is already a significant amount of academic research material available on RF WPT, RF SWIPT, and RF EH. These include waveform analysis, end-to-end system performance analysis, rectifier modeling and design, waveform optimization, beamforming algorithms, and link-level analysis [2], [7], [9], [10], [11], [12], [13]. In some cases, the presented results vary depending on the part of the RF WPT system under consideration. For instance, experimental results in [14] reveal that multisine signals yield higher receiver efficiency than orthogonal frequency-division multiplexing (OFDM) signals, chaotic signals, harmonic signals, and so on. However, while considering the nonlinearities at the transmitter, the experiments in [9] and [15] suggest that high peak-to-average power ratio (PAPR) multisine waveforms fare poorly in terms of the end-to-end efficiency of the system.

However, as mentioned above, a majority of the research work caters to the receiver side of RF WPT, which includes rectenna design, mathematical modeling, waveform design, and measurement setups. A comprehensive survey of the various rectenna topologies employed in RF WPT and RF EH is presented in [16]. The type of receiving antenna to be used varies based on the application, frequency band, and so on. While miniature on-chip antennas are employed in biomedical applications [17], [18] of RF WPT, wideband or dual-band antennas are preferred for RF EH applications [19], [20], [21]. Furthermore, the physical design of a rectenna operating at 2.4 GHz, by designing Schottky diode-based voltage rectifiers, is presented in [22] and [23]. Similarly, Duy et al. [24] present the rectenna designed specifically for the 5.8-GHz band.

The receiver efficiency in RF WPT is dependent on several parameters. In practice, a designed rectenna would have peak receiver efficiency at a certain frequency and lesser at other RF inputs. It is observed in [16] that antennas that operate at the lower end of the spectrum have higher RF-to-dc efficiency. Another important parameter that affects the design of rectennas and the resultant receiver efficiency is the impedance mismatch between the receiving antenna and the rectifier network [13], [25], which again varies with the input signal power and frequency. The combined impact of variation in input power, PAPR, and load resistance on the receiver efficiency in RF WPT is presented in [26].

Besides physical design, there are significant theoretical contributions to the mathematical modeling of energy harvesters. A majority of these are parametric power-to-power models that relate the average input power of the RF waveform to the average harvested dc power [8], [27], [28], [29] and rely on curve-fitting based on the measurement data. While Boshkovska et al. [27] present a saturation model and utilizes a sigmoid function for fitting, Chen et al. [8] present the receiver efficiency as a heuristic expression that is a function of $P_{\text{in}}^{\text{RF}}$. Similarly, two nonlinear EH models are introduced in [28] where, in both cases, the output power is a polynomial fraction of $P_{\text{in}}^{\text{RF}}$, whereas Xu et al. [29] present the output power as a simple polynomial of $P_{\text{in}}^{\text{RF}}$. Such models are very useful for determining power allocation at the transmitter [30], [31], but not at all for waveform optimization.

To be able to design a waveform suitable for RF WPT or RF SWIPT, the rectifier models need to characterize $P_{\text{out}}^{\text{dc}}$ in terms of the parameters of the transmit signal. In [32] and [33], the diode in the rectifier is modeled by approximating the Shockley equation for a single diode, whereas Abeywickrama et al. [34] present a nonlinear current–voltage model of the rectifier's diode. These models, however, do not incorporate the input impedance mismatch at the receiver, which varies with input power [13]. These models are specifically utilized for determining the optimal amplitudes [34] and phases [32] for multisine waveforms for maximizing $P_{\text{out}}^{\text{dc}}$ in RF WPT.

Furthermore, based on the mentioned power-to-power and waveform-to-power rectifier models, the problem of waveform design with complete [33], [35], partial [36], [37], [38], [39], and no [40] knowledge of the channel state information (CSI) is available in the literature. In the case of a complete absence of CSI, the transmitter could resort to transmit diversity [40]. Additionally, the problem of communication and signal design for optimizing the end-to-end transmission in RF WPT is presented in [41].

Moving on to measurement setups, a GNU Radio-based prototype test-bed for evaluating the end-to-end (i.e., dc-to-dc) performance of any digital waveform for RF WPT was showcased in [9]. Based on pilot-based channel estimation and subsequent waveform optimization, the first closed-loop WPT prototype was presented in [22] and further improved in [42]. These implementations introduce CSI feedback to the transmitter, which is utilized to optimize the amplitude of multisine tones. However, the CSI feedback is attained over a wired medium. The literature has several other RF WPT test-beds for tasks such as charging a single supercapacitor with multiple ambient sources [43], determining the digital modulation with the lowest charging time [44], devising charging protocols to regulate multiple power sources and multiple energy harvesters [45], determining the optimal orientation between transmit and receive antennas [46], studying antenna directivity as a function of source–sensor distance [47]. Furthermore, blind adaptive beamforming techniques to direct the RF energy toward the harvester were studied and implemented in a multiple-input single-output WPT test-bed in [48]. The beamformer weights are updated based on the feedback from the energy harvester to enhance the dc output. With a different approach, the concept in [49] employs distributed beamforming with multiple power sources charging a single receiver. In this case, beamforming aligns the phases of RF waves from various transmitters at the receiver,

to obtain a multisine waveform with high PAPR at the receiver input.

Coming to SWIPT test beds, an software-defined radio (SDR)-based system was presented in [50] to study rate–energy tradeoffs in SWIPT systems. Separate signals were employed for WPT and information transfer, and they were superimposed for transmission based on time-switching and power-splitting schemes. The performance of multisine and modulated OFDM signals for SWIPT was evaluated. Another SWIPT test-bed to study the performance of multisine frequency-shift keying (FSK) signals was showcased in [51]. The information is encoded in the frequency spacing of the sinusoids and thus can be decoded at the receiver without the need for a local oscillator. This encoding method allows the use of high-PAPR signals for achieving high receiver efficiency and high throughput. Both the aforementioned SWIPT test-beds utilize an ideal vector signal transceiver (VST) as a transmitter and information decoder, with the former utilizing an external power amplifier (PA) as well. A brief overview of more such test-beds is available in [52].

C. Contributions and Organization

The nonlinear waveform-to-power models [32], [33], [34], [35], [36] relate $P_{\text{out}}^{\text{dc}}$ to the incoming RF waveform $\hat{y}(t)$ and are thus suitable for waveform optimization. While Boaventura and Carvalho [32] utilize their model only for analyzing the RF WPT performance with different multisine waveforms, the waveform optimization in [33], [34], [35], and [36] is limited to the design of amplitudes and phases. The optimization thereof does not involve the design of the frequencies of the baseband signal, but instead assumes the baseband signal to be a multisine with evenly spaced frequencies. Consequently, the state-of-the-art designs are incapable of yielding an arbitrary waveform that corresponds to the global optimum as they are restricted to a multisine signal with a not-so-large number of tones. Naturally, the bandwidth constraint is also neglected. Additionally, while [32], [33], [34], [35], and [36] are seminal works, models thereof are devised with a few simplifications that may not necessarily be very practical. First, these models assume perfect input impedance matching at the receiver as they do not include a matching network between the receiving antenna and the rectifier circuit, which is usually present in commercial energy harvesters [53]. Second, the models are derived from a single-diode rectifier circuit.

Overall, there is a need for a general waveform-to-power rectifier model and nonsimplified waveform optimization. In this article, we overcome the aforementioned research gaps through the following novel contributions.

1) We present a novel rectifier model that expresses the average harvested dc power in terms of the power distribution of the envelope signal of the incident RF waveform. The proposed parametric model is independent of the underlying matching network, rectifier circuit, as well as load impedance architecture and thus is applicable for any EH receiver circuit as soon as the parameter fitting is performed based on simulation or measurement data. Thus, it takes inherently into account the impedance mismatch at the receiver input and output.
2) The proposed rectifier model accurately predicts the average harvested dc power for any waveform with a known power-level distribution function, that is, histogram in other words. The model evaluates the instantaneous rectification efficiency based on continuous-wave (CW) data and utilizes it in conjunction with the distribution function to determine the average harvested dc power for a particular waveform. We examine the receiver efficiency of different RF WPT and RF SWIPT waveforms using the proposed model to demonstrate its applicability.
3) We use the proposed rectifier model to perform general transmit-side waveform optimization to maximize the average harvested dc power at the receiver while accounting for a transmit power constraint, available channel bandwidth, and frequency-selective channel gains.
4) We present a multiband test-bed to evaluate the receiver efficiency of any digital waveform. Using this test-bed, we experimentally verify the predictions of the proposed rectifier model for various waveforms, including information-carrying phase shift keying (PSK) and quadrature amplitude modulation (QAM) signals as well as the optimized waveforms for a large number of different load resistors, varying average input RF power, six frequency bands, and three harvester circuits.

The remainder of this article is organized as follows. In Section II, we present the system model employed in this work. Afterward, we present the novel waveform-to-power rectifier model in Section III and, using it, design the optimal waveform for RF WPT in Section IV. The experimental and simulation results that verify the precision of our rectifier model and the subsequent optimization are presented in Section V. Finally, we present the conclusion of this work in Section VI.

II. System Model

In general, an RF WPT/SWIPT system comprises a digital transceiver, an external PA, and an RF EH receiver (with or without information transceiver capability). The system also incorporates a CSI feedback mechanism so that the waveform at the transmitter could be optimized over a frequency-selective channel. The digital transceiver creates $x(t)$ that is transmitted as $\hat{x}(t)$ at center frequency f_c, propagated over a wireless channel $\hat{h}(t)$, and received as $\hat{y}(t)$. The modeling applies to both WPT and SWIPT, but this article is presented in the context of EH from $\hat{y}(t)$ despite it may contain information too.

Without loss of generality, we assume that the digital baseband signal to be transmitted is a complex-valued N-tone multisine waveform given by

$$\begin{aligned} x(t) &= x_I(t) + jx_Q(t) \\ &= \sum_{n=1}^{N} A_n \exp\left[j2\pi f_n t + j\phi_n\right] \end{aligned} \tag{1}$$

where A_n, f_n, and ϕ_n represent the amplitude, the baseband frequency, and the phase of the nth tone, respectively.

A multisine waveform can approximate (or, if $N \to \infty$, exactly represent) an interval of any signal $x(t)$ when interpreted as a Fourier series, which justifies the assumption.

The corresponding RF signal at the transmitter can be expressed as

$$\hat{x}(t) = \sqrt{2}\sum_{n=1}^{N} A_n \cos(2\pi(f_c + f_n)t + \phi_n) \tag{2}$$

and the averagetransmitted RF power is given as

$$P_{\text{out}}^{\text{RF}} = \frac{1}{T}\int_0^T \hat{x}^2(t)dt = \frac{1}{T}\int_0^T |x(t)|^2 dt = \sum_{n=1}^{N} A_n^2 \tag{3}$$

where T is the time period or interval duration of the modulating signal. The result of (3) applies to multisines irrespective of individual A_n, f_n, or ϕ_n (so long as f_n are distinct for all n) as a direct consequence of Parseval's theorem. We let P_{Tx} denote the transmit power limit, such that $P_{\text{out}}^{\text{RF}} \leq P_{\text{Tx}}$.

The RF signal traverses a wireless medium with channel response $\hat{h}(t)$ and arrives at the energy harvester as

$$\begin{aligned}\hat{y}(t) &= \hat{h}(t) * \hat{x}(t) + \hat{w}(t)\\ &\approx \hat{h}(t) * \hat{x}(t)\\ &= \sum_{n=1}^{N} \hat{A}_n \cos\big(2\pi(f_c + f_n)t + \hat{\phi}_n\big)\end{aligned} \tag{4}$$

where the receiver noise $\hat{w}(t)$ can be considered to be negligible from the EH perspective since the noise power level is way below the sensitivity threshold of RF energy harvesters [53], [55]. The receiver noise is similarly neglected in other such research works on RF WPT, assiduously summarized in [7].

The impact of the channel on the individual multisine tones is represented as $\hat{A}_n = A_n|H_n|$ and $\hat{\phi}_n = \phi_n + \angle H_n$. The baseband signal for the received RF signal $\hat{y}(t)$ can be described as

$$y(t) = \sum_{n=1}^{N} \hat{A}_n \cos\big(2\pi f_n t + \hat{\phi}_n\big) \tag{5}$$

while the corresponding envelope signal is given as $\sqrt{2}|y(t)|$. Next, the instantaneous power of this envelope signal can be expressed as

$$p(t) = 2|y(t)|^2 \tag{6}$$

while the average input RF power of the received signal, using (4) and (3), is given as

$$\begin{aligned}P_{\text{in}}^{\text{RF}} &= \mathcal{E}\big\{\hat{y}^2(t)\big\}\\ &= \mathcal{E}\Big\{\big(\hat{h}(t) * \hat{x}(t)\big)^2\Big\}\\ &= \mathcal{E}\big\{\hat{h}^2(t)\big\} \cdot \mathcal{E}\big\{\hat{x}^2(t)\big\}\\ &= \mathcal{E}\big\{|h(t)|^2\big\} \cdot \mathcal{E}\big\{|x(t)|^2\big\}\end{aligned} \tag{7}$$

where $x(t)$ is any complex baseband waveform and $h(t)$ is the complex baseband channel equivalent of $\hat{h}(t)$. The third step in (7) arrives from the assumption that the signal and channel are uncorrelated. For a frequency-selective slow-fading channel, the average received RF power can be denoted as

$$P_{\text{in}}^{\text{RF}} = \sum_{n=1}^{N} A_n^2 |H_n|^2. \tag{8}$$

After rectification, the input signal $\hat{y}(t)$ generates an output voltage $v_{\text{out}}(t)$ across the load resistor R_L. The harvested dc voltage ($V_{\text{out}}^{\text{dc}}$) is the root mean square (rms) value of $v_{\text{out}}(t)$, given as

$$V_{\text{out}}^{\text{dc}} = \sqrt{\frac{1}{T}\int_0^T v_{\text{out}}^2(t)dt}. \tag{9}$$

Correspondingly, the instantaneous output power is given as $([v_{\text{out}}^2(t)]/R_L)$ and the harvested dc power is given as

$$P_{\text{out}}^{\text{dc}} = \frac{\big(V_{\text{out}}^{\text{dc}}\big)^2}{R_L}. \tag{10}$$

Finally, the overall receiver efficiency is computed as

$$\begin{aligned}\eta &= \frac{P_{\text{out}}^{\text{dc}}}{P_{\text{in}}^{\text{RF}}}\\ &= \frac{\big(V_{\text{out}}^{\text{dc}}\big)^2}{R_L \sum_{n=1}^{N} A_n^2 |H_n|^2}.\end{aligned} \tag{11}$$

III. Novel Rectifier Model

In this section, we propose a novel *waveform-to-EH* model for an RF EH receiver.[1] The proposed model relates the average harvested dc power to the characteristics of the input RF waveform, and not to just its average RF input power like typical nonlinear models. The proposed model incorporates the impact of the matching network along with the rectifier circuit, for a given load resistor. In comparison with the existing nonlinear RF EH models, the novelty of the proposed *waveform-to-EH* model is demonstrated in Table I.

Let us first briefly explain the notion behind this rectifier model: Given a baseband-modulated RF signal, where f_c is sufficiently higher than the highest $|f_n|$, the individual cycles (or a few of them) can approximately be represented as single-tone sinusoids with a constant amplitude. The constant amplitude here is the magnitude of the modulating signal at that time instant. Each such single-tone sinusoid on traversing through the RF EH circuit results in a certain rectified dc rms voltage. The overall average harvested dc power is then given by the average of these rectified dc rms powers over the time period T of the input RF signal, which requires specifying only the amplitude distribution of the received signal. The above idea is supported by the measurement observations, which reveal that the rectified signal $v_{\text{out}}(t)$ follows the envelope of the baseband signal $y(t)$. Accordingly, we propose that the instantaneous output power at each time instant is obtained by feeding the rectifier a single-tone input, whose input power is determined by the magnitude of $y(t)$ at that time instant.

[1]The RF EH receiver employed in this study comprises a diode-based rectifier that is only utilized for RF-to-dc conversion—the rectifier under consideration does not serve the purpose of demodulating communication signals such as quadrature phase-shift keying (QPSK), QAM, and OFDM.

TABLE I
COMPARISON OF NONLINEAR RECTIFIER MODELS FOR RF WPT

Work	**Model type**	**Notion**	$P_{\text{in}}^{\text{RF}}$ **range**	**Input impedance mismatch at receiver**	**Optimize transmit power**	**Waveform design**			
						A_n	ϕ_n	f_n	W
[27], [30]	Parametric	$P_{\text{out}}^{\text{DC}}$ is a saturation dependent logistic function of $P_{\text{in}}^{\text{RF}}$	Saturation region (circuit dependent)	Incorporated	✓	x	x	x	x
[8]	Parametric	η is a heuristic polynomial fraction of $P_{\text{in}}^{\text{RF}}$	-28 dBm to 0 dBm	Incorporated	x	x	x	x	x
[28]	Parametric	$P_{\text{out}}^{\text{DC}}$ is a saturation based polynomial fraction of $P_{\text{in}}^{\text{RF}}$	-5 dBm and above	Incorporated	x	x	x	x	x
[29]	Parametric	$P_{\text{out}}^{\text{DC}}$ is a heuristic polynomial of $P_{\text{in}}^{\text{RF}}$	-5 dBm and above	Incorporated	✓	x	x	x	x
[32]	Approximation	$v_{\text{out}}(t)$ is expressed as a polynomial of $y(t)$ by approximating the Shockley-diode equation	-20 dBm to 0 dBm	Ignored	x	x	x	x	x
[33], [36]	Approximation	$v_{\text{out}}(t)$ is expressed as a polynomial of $y(t)$ by approximating the Shockley-diode equation	-30 dBm to 20 dBm (practically validated at -20 dBm)	Ignored	✓	✓	✓	x	x
[34], [35]	Deterministic (numerically)	A semi-closed-form expression for $v_{\text{out}}(t)$ in terms of $y(t)$ by using the Shockley-diode equation for a single-diode circuit	-3 dBm to 5 dBm	Ignored	✓	✓	✓	x	x
Proposed	Probabilistic	The rectified signal follows the envelope of the baseband signal	-30 dBm to 20 dBm	Incorporated	✓	✓	✓	✓	✓

For the mathematical representation of the model, it is convenient to consider time $\mathcal{T}$ to be a random variable, which is uniformly distributed within one time period interval of the modulating signal. This is because the model is based on only the statistical distribution of the input signal's instantaneous power while the precise temporal evolution over time is irrelevant. Consequently, $y(\mathcal{T})$ and $p(\mathcal{T})$ become random variables, which we denote simply as $\mathcal{Y}$ and $\mathcal{P}$, respectively, for brevity. The instantaneous output power is given as $\eta(\mathcal{P}) \cdot \mathcal{P}$, where $\eta(\mathcal{P})$ is the efficiency of the receiver for instantaneous input power $\mathcal{P}$ that captures the behavior of the entire receiver circuit, including the antenna port, matching network, and the rectifier circuit for a given load resistor R_L.

In summary, as experiments corroborate in Section V, the overall harvested dc power can be represented as

$$\begin{aligned} P_{\text{out}}^{\text{dc}} &= \mathcal{E}\{\eta(\mathcal{P}) \cdot \mathcal{P}\} \\ &= \int_0^\infty \eta(p) \cdot p \cdot f_{\mathcal{P}}(p) dp \end{aligned} \tag{12}$$

where $f_{\mathcal{P}}(p)$ denotes the probability density function of the instantaneous power of the envelope signal. Equation (12) represents the proposed rectifier model based on the power distribution of the baseband/modulating signal's envelope. The model predicts the output dc power/voltage for any baseband waveform $y(t)$, given its amplitude/power distribution $f_{\mathcal{P}}(p)$, and $\eta(p)$ that contains the parameters of the model that characterize the receiver. In Sections III-A and III-B, we will explain how to estimate them before using the model.

A. Determination of $\eta(p)$

The parametric model in (12) relies on having the knowledge of the efficiency of the rectifier for each input power, that is, the model parameters. To achieve this, one should first determine the rectifier efficiency at M input power points either through measurements or simulations. Let us denote the measurement data points and estimated parameters with a tilde, for them to be discernible.

At each of the k input power points ($k \in [1, M]$), a single-tone input is transmitted, for which the envelope signal is basically constant, so, $p_k = \tilde{P}_{\text{in}}^{\text{RF}}[k]$ and $f_{\mathcal{P}}(p) = \delta(p - p_k)$. Thus, for each input power level $\tilde{P}_{\text{in}}^{\text{RF}}[k]$, we measure $\tilde{P}_{\text{out}}^{\text{dc}}[k]$ and obtain the efficiency using (12) simply as

$$\tilde{\eta}_k = \frac{\tilde{P}_{\text{out}}^{\text{dc}}[k]}{\tilde{P}_{\text{in}}^{\text{RF}}[k]}. \tag{13}$$

Using this set of discrete $\tilde{\eta}_k$, a smooth curve for $\tilde{\eta}(p)$ can be achieved by using piecewise polynomial interpolation as

$$\tilde{\eta}(p) = \sum_{l=0}^{R} a_{i,l}(p - p_i)^l \tag{14}$$

for $p_i \le p \le p_{i+1}$, where $i \in [1, M-1]$, and R is the degree of the piecewise polynomial. To avoid discontinuities in $\tilde{\eta}(p)$ at the internal points p_i ($i \in [2, M-1]$), we can opt for higher-order spline interpolation such as the widely used cubic spline. The coefficients $a_{i,l}$ in (14) are obtained from the constraints on the polynomial in (14) per [56].

If (14) were to be represented with a cubic spline ($R = 3$), the coefficients $a_{i,2}$ would be given as solution to the equations

$$\begin{aligned} a_{i-1,2}(p_i - p_{i-1}) + 2a_{i,2}(p_{i+1} - p_{i-1}) + a_{i+1,2}(p_{i+1} - p_i) \\ = 3\frac{\tilde{\eta}_{i+1} - \tilde{\eta}_i}{(p_{i+1} - p_i)} - 3\frac{\tilde{\eta}_i - \tilde{\eta}_{i-1}}{(p_i - p_{i-1})}. \end{aligned} \tag{15}$$

With M input power points, we have M such equations which would yield M unique $a_{i,2}$ coefficients. Once the value of $a_{i,2}$ is attained, the remaining coefficients can be computed as

$$\begin{aligned} a_{i,0} &= \tilde{\eta}_i \\ a_{i,1} &= \frac{\tilde{\eta}_{i+1} - \tilde{\eta}_i}{(p_{i+1} - p_i)} - \frac{(p_{i+1} - p_i)}{3} \cdot \left(2a_{i,2} + a_{i+1,2}\right) \\ a_{i,3} &= \frac{a_{i+1,2} - a_{i,2}}{3(p_{i+1} - p_i)}. \end{aligned} \tag{16}$$

Thus, by varying the input power levels of a single-tone sinusoid at RF, recording the corresponding rectifier efficiency, and then interpolating for the intermediate points, we attain a continuous curve for estimated $\tilde{\eta}(p)$ using (14).

B. Determination of $f_{\mathcal{P}}(p)$

The other information needed for computing $P_{\text{out}}^{\text{dc}}$ for any given baseband waveform using (12) is the probability density function of the instantaneous power of the baseband waveform. It can be computed as follows considering a baseband waveform $\mathcal{Y} = y(\mathcal{T})$, which is a function of random variable $\mathcal{T}$.

In the case that it is not possible to express $\mathcal{Y}$ as an equation, its $f_{\mathcal{P}}(p)$ can be estimated numerically from its normalized histogram, given that the number of samples of T is very large and the number of histogram bins is also huge. Now, if g_i is the normalized histogram value for the bin $p_i < p \leq p_{i+1}$ ($i \in [1, \text{number of bins}]$), with midpoint $\check{p}_i$, then the discrete probability is given as $g_i \delta(p - \check{p}_i)$, and the corresponding estimated probability density function is given by

$$\tilde{f}_{\mathcal{P}}(p) = \sum_i g_i \delta\big(p - \check{p}_i\big). \tag{17}$$

This approach is useful when $y(t)$ is available as a complex-valued sample sequence from simulations or measurements.

In the other case, when the equation $\mathcal{Y} = y(\mathcal{T})$ is known and used, first the corresponding cumulative distribution function using (6) is given as

$$\begin{aligned} F_{\mathcal{P}}(p) &= \Pr(\mathcal{P} \leq p) \\ &= \Pr\left(-\sqrt{\frac{p}{2}} \leq \mathcal{Y} \leq \sqrt{\frac{p}{2}}\right) \\ &= F_{\mathcal{T}}\left(y^{-1}\left(\sqrt{\frac{p}{2}}\right)\right) - F_{\mathcal{T}}\left(y^{-1}\left(-\sqrt{\frac{p}{2}}\right)\right) \end{aligned} \tag{18}$$

where $\mathcal{T} \sim \cup(0, T]$. Thus, the probability density function is given as

$$f_{\mathcal{P}}(p) = \frac{1}{T} \cdot \left(\frac{d}{dp} y^{-1}\left(\sqrt{\frac{p}{2}}\right) - \frac{d}{dp} y^{-1}\left(-\sqrt{\frac{p}{2}}\right)\right). \tag{19}$$

If the modulating signal equation $\mathcal{Y} = y(\mathcal{T})$ is not invertible or monotonic as required in (19), then we can resort to numerical computation of $\tilde{f}_{\mathcal{P}}(p)$ as discussed in the previous case.

Let us now present two special cases when $f_{\mathcal{P}}(p)$ is exactly known. These are the two-multisine and three-multisine modulating signals, where the adjacent tones have equal amplitude and the same phase, as defined in the experimental setup in [9]. The modulating signal in these cases is given by as

$$\mathcal{Y} = \begin{cases} \sqrt{2P_{\text{in}}^{\text{RF}}} \cos\big(\pi \Delta_f \mathcal{T}\big), & \text{when } N = 2 \\ \sqrt{P_{\text{in}}^{\text{RF}}/3}\big[1 + 2\cos\big(2\pi \Delta_f \mathcal{T}\big)\big], & \text{when } N = 3. \end{cases} \tag{20}$$

The corresponding cumulative density function is given as $F_{\mathcal{P}}(p) =$

$$\begin{cases} \dfrac{1}{2\pi \Delta_f} F_{\mathcal{T}}\left(\cos^{-1}\left(\dfrac{p}{P_{\text{in}}^{\text{RF}}} - 1\right)\right), & \text{when } N = 2 \\ \dfrac{1}{2\pi \Delta_f} F_{\mathcal{T}}\left(\cos^{-1}\left(\sqrt{\dfrac{3p}{4P_{\text{in}}^{\text{RF}}}} - \dfrac{1}{2}\right)\right. & \\ \qquad \left. - \cos^{-1}\left(-\sqrt{\dfrac{3p}{4P_{\text{in}}^{\text{RF}}}} - \dfrac{1}{2}\right)\right), & \text{when } N = 3 \end{cases} \tag{21}$$

where $\mathcal{T} \sim \cup(0, (1/\Delta_f)]$. Thus, the exact probability density function is given as $f_{\mathcal{P}}(p) =$

$$\begin{cases} \dfrac{1}{2\pi\sqrt{p}\sqrt{2P_{\text{in}}^{\text{RF}} - p}}, & N = 2 \\ \dfrac{1}{4\pi\sqrt{p}} \left(\dfrac{1}{\sqrt{\left(\sqrt{3P_{\text{in}}^{\text{RF}}} - \sqrt{p}\right)\left(\sqrt{P_{\text{in}}^{\text{RF}}/3} + \sqrt{p}\right)}} \right. & \\ \qquad \left. + \dfrac{1}{\sqrt{\left(\sqrt{3P_{\text{in}}^{\text{RF}}} + \sqrt{p}\right)\left(\sqrt{P_{\text{in}}^{\text{RF}}/3} - \sqrt{p}\right)}} \right), & N = 3 \end{cases} \tag{22}$$

where $0 \leq p \leq N P_{\text{in}}^{\text{RF}}$. Unfortunately, $\mathcal{Y} = y(\mathcal{T})$ is not invertible for multisines with higher N.

IV. Waveform Optimization

In Section III, we presented a novel rectifier model that yields $P_{\text{out}}^{\text{dc}}$ for any given waveform. In this section, we determine the receive and transmit waveforms that are optimal for RF WPT based on the model.

A. Optimization Problem Formulation

The primary goal of any RF WPT system is to maximize $P_{\text{out}}^{\text{dc}}$ with the available energy and spectrum resources at the transmitter side. This can be broadly expressed in the form of an optimization problem as

$$\begin{aligned} &\max_{x(t)} \ P_{\text{out}}^{\text{dc}} \\ &\text{s.t.} \ \frac{1}{T}\int_0^T |x(t)|^2 dt = P_{\text{Tx}} \\ &\qquad \frac{1}{T}\int_{-W/2}^{W/2} |X(f)|^2 df \leq \alpha P_{\text{Tx}} \end{aligned} \tag{23}$$

where

$$X(f) = \int_{-\infty}^{\infty} x(t) \cdot e^{-j2\pi f t} dt \tag{24}$$

represents the Fourier transform of $x(t)$, having $0 < \alpha < 1$ times the instantaneous bandwidth W.[2] The optimization problem in (23) is purposed to ascertain the optimal transmit waveform $x^*(t)$. The first constraint ensures that the RF WPT source transmits at the maximum available power level (P_{Tx}), while the second constraint ensures that the signal resides within the allotted channel of bandwidth W.

If we now express the transmit waveform in a general form as defined in (1), the optimization problem narrows down to a waveform optimization problem where the multisine amplitude, frequency, and phase are optimized to yield maximum $P_{\text{out}}^{\text{dc}}$. Moreover, given a wireless medium, there is an additional constraint on the spectral bandwidth of the waveform. The modified optimization problem can be expressed as

$$\begin{aligned} \max_{\{A_n, f_n, \phi_n\}} \quad & P_{\text{out}}^{\text{dc}} \\ \text{s.t.} \quad & \sum_{n=1}^{N} A_n^2 = P_{\text{Tx}} \\ & |f_n| \leq \frac{W}{2} \quad \forall n \in [1, N] \end{aligned} \tag{25}$$

where $\sum_{n=1}^{N} A_n^2$ denotes the transmit power as defined in (3). Again, the two constraints ensure the transmit power and bandwidth limits are adhered, respectively. However, for yielding the globally optimum waveform with respect to (23), the above optimization problem requires also N to approach infinity.

We shall utilize the following approach for optimizing the waveform at the transmitter. First, we determine the optimal envelope signal at the harvester input which maximizes $P_{\text{out}}^{\text{dc}}$. Afterward, by incorporating the effect of a slow-fading frequency-selective channel, we choose the transmit waveform parameters that would yield the optimal waveform at the receiver input, while complying with the constraints.

B. Optimization Problem at the Receiver

The novel rectifier model presented in (12) relies on the power distribution of the envelope signal and thus is suitable to be used for waveform optimization at the receiver. If we observe the model in (12), we realize that $P_{\text{out}}^{\text{dc}}$ is dependent on $\eta(p)$ and $f_{\mathcal{P}}(p)$, with the former pertaining to the energy harvester in use. Thus, only the latter parameter can be controlled and optimized to maximize $P_{\text{out}}^{\text{dc}}$, which is the power distribution of the input RF waveform $f_{\mathcal{P}}(p)$. The waveform optimization problem at the receiver can thus be presented as

$$\begin{aligned} \max_{f_{\mathcal{P}}(p) \geq 0} \quad & \int_0^{\infty} \eta(p) \cdot p \cdot f_{\mathcal{P}}(p) dp \\ \text{s.t.} \quad & \int_0^{\infty} p \cdot f_{\mathcal{P}}(p) dp = P_{\text{in}}^{\text{RF}} \\ & \int_0^{\infty} f_{\mathcal{P}}(p) dp = 1 \end{aligned} \tag{26a}$$

[2]The parameter $1 - \alpha$ signifies the relative amount of spectral leakage permitted in the adjacent frequency bands. The higher the value of α, the wider is the measured bandwidth of the transmitted signal.

or equivalently, when $f_{\mathcal{P}}(p)$ is implicitly constrained to be a proper probability density function, as simply

$$\begin{aligned} \max_{f_{\mathcal{P}}(p)} \quad & \mathcal{E}\{\eta(\mathcal{P}) \cdot \mathcal{P}\} \\ \text{s.t.} \quad & \mathcal{E}\{\mathcal{P}\} = P_{\text{in}}^{\text{RF}} \end{aligned} \tag{26b}$$

which should yield the optimal power distribution $f_{\mathcal{P}}^*(p)$ for the envelope signal that maximizes $P_{\text{out}}^{\text{dc}}$ in RF WPT. It must be noted that any number of waveforms could have the same $f_{\mathcal{P}}^*(p)$. Among those, we select the optimal waveform that satisfies the constraints in (23) or (25) and other criteria.

To maximize $P_{\text{out}}^{\text{dc}}$ at a given $P_{\text{in}}^{\text{RF}}$, the receiver must operate at maximum η at that $P_{\text{in}}^{\text{RF}}$. Now, it is evident from Fig. 1(c) that the EH receiver yields maximum η at only one unique $P_{\text{in}}^{\text{RF}}$, say $\bar{p}$, for a given R_L. Consequently, the upper bound for (12) is given as

$$\begin{aligned} \mathcal{E}\{\eta(\mathcal{P}) \cdot \mathcal{P}\} &\leq \begin{cases} \mathcal{E}\{\eta(\bar{p}) \cdot \mathcal{P}\}, & P_{\text{in}}^{\text{RF}} \leq \bar{p} \\ \eta(\mathcal{E}\{p\}) \cdot \mathcal{E}\{p\}, & P_{\text{in}}^{\text{RF}} > \bar{p} \end{cases} \\ &= \begin{cases} \eta(\bar{p}) \cdot P_{\text{in}}^{\text{RF}}, & P_{\text{in}}^{\text{RF}} \leq \bar{p} \\ \eta\left(P_{\text{in}}^{\text{RF}}\right) \cdot P_{\text{in}}^{\text{RF}}, & P_{\text{in}}^{\text{RF}} > \bar{p} \end{cases} \end{aligned} \tag{27}$$

where

$$\bar{p} = \arg\max_{p} \eta(p) \tag{28}$$

is the instantaneous input power of the envelope signal at which maximum efficiency is attained. Furthermore, when $P_{\text{in}}^{\text{RF}} > \bar{p}$, we can assume that the product $\eta(\mathcal{P}) \cdot \mathcal{P}$ to be concave and apply Jensen's inequality, which is corroborated by actual experimental data, as shown in Fig. 1(b).

The upper bound implies that to maximize $P_{\text{out}}^{\text{dc}}$, the received envelope signal ought to have just one nonzero power level at $\bar{p}$ or $P_{\text{in}}^{\text{RF}}$. Consequently, we propose a power density function at the receiver, for an input signal with average RF input power $P_{\text{in}}^{\text{RF}}$, given as

$$f_{\mathcal{P}}^*(p) = \left(1 - \mu^*\right) \cdot \delta(p) + \mu^* \cdot \delta\left(p - \frac{P_{\text{in}}^{\text{RF}}}{\mu^*}\right) \tag{29}$$

where the parameter

$$\mu^* = \begin{cases} \dfrac{P_{\text{in}}^{\text{RF}}}{\bar{p}}, & P_{\text{in}}^{\text{RF}} \leq \bar{p} \\ 1, & P_{\text{in}}^{\text{RF}} > \bar{p} \end{cases} \tag{30}$$

represents the optimal relative duration of the power level.

Employing the density function proposed in (29) and the subsequent μ^* defined in (30), the average harvested dc power is given as

$$\begin{aligned} P_{\text{out}}^{\text{dc}} &= \mathcal{E}\{\eta(\mathcal{P}) \cdot \mathcal{P}\} \\ &= \int_0^{\infty} \eta(p) \cdot p \cdot \left[\left(1-\mu^*\right) \cdot \delta(p) + \mu^* \cdot \delta\left(p - \frac{P_{\text{in}}^{\text{RF}}}{\mu^*}\right)\right] dp \\ &= \eta\left(\frac{P_{\text{in}}^{\text{RF}}}{\mu^*}\right) \cdot P_{\text{in}}^{\text{RF}}. \end{aligned} \tag{31}$$

On substituting (30) in (31) and then comparing with (27), it is clear that (29) attains the upper bound and is thus an optimal solution for maximizing $P_{\text{out}}^{\text{dc}}$. The proposed density function represents a pulsed RF wave with duty cycle μ^*.

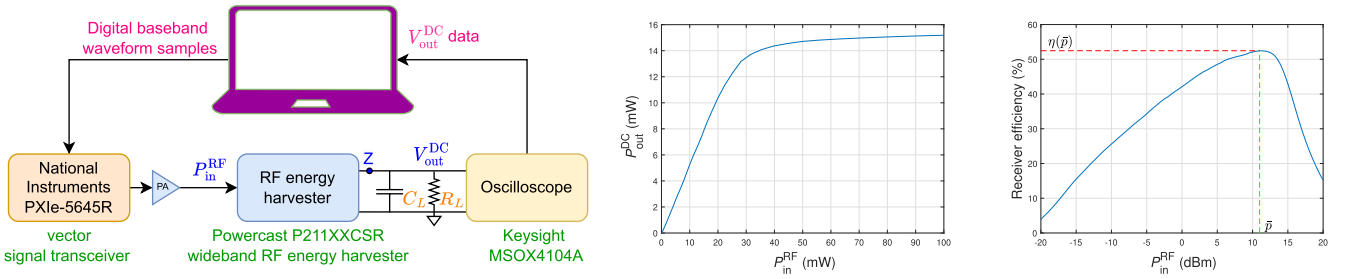

(a) (b) (c)

Fig. 1. Block diagram of the presented RF WPT system along with an example of measured harvested dc power ($P_{\text{out}}^{\text{dc}}$) and the corresponding receiver efficiency (η) for a single sinusoid RF input at 879.5 MHz. The receiver is an off-the-shelf multiband rectifier with $R_L = 3.3$ kΩ and $C_L = 15$ pF. The maximum receiver efficiency $\eta(\bar{p}) \approx 52\%$ is achieved when $P_{\text{in}}^{\text{RF}} = \bar{p} \approx 11$ dBm. When considering simultaneous power and data transfer, the RF WPT system depicted in (a) is part of a more generic RF SWIPT system shown in [54, Fig. 1]. Such an RF SWIPT system constitutes separate signal paths for information decoding and EH. (a) General block diagram. (b) Measured average harvested dc power. (c) Receiver efficiency.

This completes the optimization problem at the receiver. Next, we revert back to the original problem (25) of determining the optimal waveform at the transmitter.

C. Optimal Waveforms at the Transmitter

The optimal distribution at the receiver input as described in (29) provides no information about the frequencies of the optimal baseband signal. It only implies that the optimal envelope signal at the transmitter is also a rectangular pulse. At the transmitter side, the bandwidth constraint in (23) is critical, for which we assume that the spectrum regulations specify α as a parameter for spectral containment and the maximum permissible absolute pulse duration $\tau_{\max}$. The parameter $\tau_{\max}$ allows us to determine the minimum instantaneous bandwidth $\overline{W}_{\min}$ for the transmitted signal as follows.

Now, with a pulsed RF signal, there is scope for frequency modulation at the baseband. However, to attain a high-PAPR pulse at RF, we would need the absolute pulse duration to be as small as feasible, say $\tau_{\min}$. This requires minimal frequency variation at the baseband. Consequently, to maximize the power received through wireless propagation, we choose the optimal baseband transmit frequency as

$$f^* = \arg\max_f |H(f)|^2 \quad \text{s.t. } f \in \left[f_L + \frac{\overline{W}_{\min}}{2}, f_U - \frac{\overline{W}_{\min}}{2} \right] \tag{32}$$

where $H(f)$ represents the Fourier transform of the baseband equivalent of channel $\hat{h}(t)$, while f_L and f_U represent the lower and upper boundaries of the available channel bandwidth $W = f_U - f_L$, respectively. The total guard bandwidth $\overline{W}_{\min}$ at the edges of W ensures that the spectral leakage to the adjacent bands is restricted to $(1-\alpha)P_{\text{Tx}}$, as required in (23).

Now, the optimal baseband signal at the transmitter can be given by

$$x^*(t) = \exp\left[j2\pi f^* t + j\phi^* \right] \cdot r(t) \tag{33}$$

where

$$r(t) = \begin{cases} A, & 0 < t < \tau \\ 0, & \tau < t < T \\ r(t + kT), & k \in \mathbb{Z} \end{cases} \tag{34}$$

represents a train of rectangular pulses with absolute pulse duration $\tau_{\min} \le \tau \le \tau_{\max}$ and repetition interval T. The optimal duty cycle μ^* in (30) can, thus, also be represented as

$$\mu^* = \frac{\tau}{T} \tag{35}$$

and, consequently, the optimal amplitude from the first constraint in (23) is given as

$$A = \sqrt{\frac{P_{\text{Tx}}}{\mu^*}}. \tag{36}$$

Now, to complete the waveform optimization problem at the transmitter, we ought to determine the parameters $\overline{W}_{\min}$, $\tau_{\min}$, T, and ϕ^*. We start by determining $\overline{W}_{\min}$ and $\tau_{\min}$ utilizing the second constraint in (23), based on the available transmit power P_{Tx} and α. Consider the Fourier transform of $x^*(t)$ given as

$$\left| X\left(f^* + f\right) \right| = |A\tau \operatorname{sinc}(\tau f \pi)|. \tag{37}$$

Now, for any general bandwidth B, on substituting (37) in the second constraint of (23) and using (36), we get

$$\begin{aligned} \alpha P_{\text{Tx}} &\ge \frac{1}{T} \int_{-B/2}^{B/2} |A\tau \operatorname{sinc}(\tau f \pi)|^2 df \\ \alpha \frac{A^2\tau}{T} &\ge \frac{2A^2\tau^2}{T} \int_0^{B/2} \operatorname{sinc}^2(\tau f \pi) df \\ \alpha &\ge \sum_{m=0}^{\infty} \frac{(-1)^m (2\pi\tau B)^{2m+1}}{\pi(2m+1)(2m+2)!}. \end{aligned} \tag{38}$$

While it is not possible to invert (38) to obtain an expression for τ in terms of B, or vice versa, we can do so numerically and the results are shown in Fig. 2. Let us define a function $q(\tau, B)$ as

$$q(\tau, B) = \sum_{m=0}^{\infty} \frac{(-1)^m (2\pi\tau B)^{2m+1}}{\pi(2m+1)(2m+2)!} - \alpha. \tag{39}$$

Then $\overline{W}_{\min}$ in terms of $\tau_{\max}$ is the solution to

$$q\left(\tau_{\max}, \overline{W}_{\min}\right) = 0 \tag{40}$$

while $\tau_{\min}$ in terms of f^* is the solution to

$$q\left(\tau_{\min}, 2\min\left\{f^* - f_L, f_U - f^*\right\}\right) = 0. \tag{41}$$

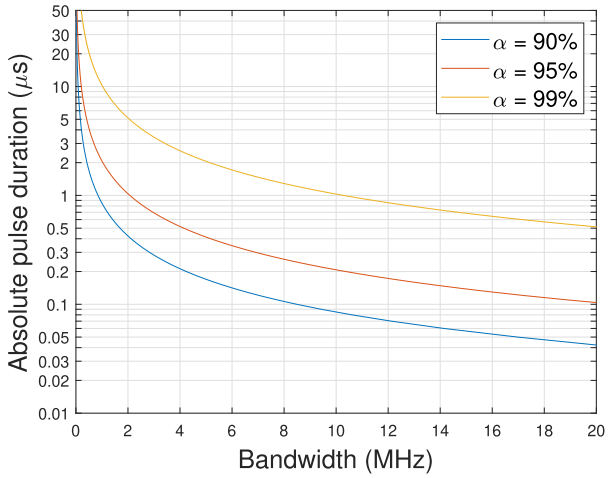

Fig. 2. Absolute pulse duration corresponding to available instantaneous bandwidth for different values of parameter α as defined in (23).

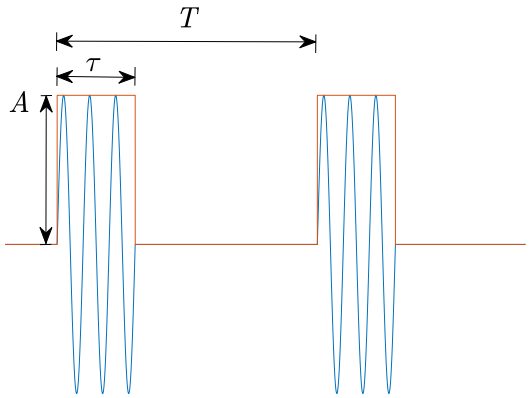

Fig. 3. Optimal signal at the transmitter: a pulsed RF signal with absolute pulse duration τ, repetition interval T, and amplitude A, with the baseband frequency $f^* \ll f_c$.

$\overline{W}_{\min}$ for any τ is demonstrated in Fig. 2. Moreover, it is evident in Fig. 2 that increasing α greatly impacts $\tau_{\min}$. We observe that for instantaneous channel bandwidth up to 10 MHz, $\tau_{\min} \approx 0.1$ μs for even 90% occupied bandwidth. This implies that transmitting multiple short pulses ($\tau < 0.1$ μs) is not feasible, given the bandwidth and α constraints. In a practical RF WPT system, the transmitter always transmits at the maximum permissible power P_{Tx} while utilizing the entire available bandwidth. Thus, the minimum pulse duration $\tau = \tau_{\min}$ obtained from (41) is likely the best choice in practice.

Next, the repetition interval T is obtained using (35) when τ is chosen. The determination of ϕ^* is insignificant from an RF WPT perspective and thus the task of waveform optimization at the transmitter is complete. The optimal signal is a pulsed RF as shown in Fig. 3. The transmit waveform can carry information through phase modulation, such as M-PSK, where the amplitude of the signal stays constant. Thus, a pulsed M-PSK signal, or more generally, a *pulsed continuous phase modulation* signal is suitable for RF SWIPT.

Furthermore, it is essential to note that while the optimal envelope signal at the transmitter is a rectangular wave, multipath propagation through a wireless medium ensures that the envelope signal at the receiver varies slightly from a rectangular wave due to delay spread. However, from an RF WPT perspective, the distant multipath components are already very insignificant due to the higher path loss they suffer and thus can be neglected here.

TABLE II
HARDWARE CONFIGURATION FOR THE TEST-BED

External PA	Mini-Circuits ZHL-4240+ [57]
RF energy harvester	Powercast P211XXCSR [53]
VST	National Instruments PXIe-5645R [58]
Oscilloscope	Keysight MSOX4104A [59]
RF power meter	Rohde & Schwarz NRP-Z11 [60]

V. EXPERIMENTAL RESULTS AND OBSERVATIONS

In this section, we present the experimental results verifying the theoretical results of Sections III and IV and discuss the various observations. First, we present an overview of the experimental test-bed setup developed for this work. Second, we showcase the measurement results that corroborate the efficacy of the proposed novel rectifier model for RF WPT signals such as a CW, multisine signal, Gaussian noise, pulsed RF, as well as RF SWIPT signals such as single-carrier (SC) M-PSK, SC QAM, OFDM QPSK, and OFDM QAM. Finally, we introduce experimental results that validate the superior performance of the optimal pulsed RF waveform for RF WPT.

A. Measurement Setup

A general block diagram of the test-bed used in this research work is presented in Fig. 1(a). The test-bed comprises a computer, a VST, an external PA, an RF energy harvester accompanied by load resistance (R_L), load capacitance (C_L), and an oscilloscope. The primary purpose of the test-bed is to determine the receiver efficiency η for the test waveforms. The receiver efficiency is determined as follows.

A computer, equipped with MATLAB software, generates the digital baseband waveforms and sends them to a VST, which generates an analog RF waveform for transmission. The internal power amplification of the VST is not sufficient for encompassing the entire power range of the RF energy harvester, so we employ an external PA to generate the final output RF signal with average power $P_{\text{out}}^{\text{RF}}$. The RF signal is transmitted to the RF energy harvester over a wired medium.[3] The received RF signal at the input of the RF EH has an average power $P_{\text{in}}^{\text{RF}}$. The RF energy harvester comprises a matching network followed by a Schottky-diode-based rectifier, which converts the incident RF energy to dc energy. The dc rms value of the rectified waveform ($V_{\text{out}}^{\text{dc}}$) is measured

[3]This research work primarily focuses on the receiver side of an RF WPT/SWIPT system. Moreover, we experimentally evaluate the receiver efficiency for a multiband receiver with six RF bands [53], of which five bands are utilized for commercial wireless communications. Hence, we avoid wireless measurements to avert any interference in the licensed RF bands. Additionally, it was observed in [9] that for a few MHz bandwidth in the 863–873-MHz European ISM band, the wireless channel is essentially flat and is well approximated with a path loss channel model, such as a wired medium.

TABLE III
OPERATIONAL PARAMETERS FOR THE EXPERIMENTS WITH THE MULTIBAND RECTIFIER

Parameter	Details
Frequency band (center frequency f_c)	$1: 824-849$ MHz (836.5 MHz) $2: 865-894$ MHz (879.5 MHz) $3: 880-928$ MHz (904 MHz) $4: 1.710-1.785$ GHz (1.7475 GHz) $5: 1.85-1.91$ GHz (1.88 GHz) $6: 2.4-2.5$ GHz (2.45 GHz)
$P_{\text{in}}^{\text{RF}}$	$[-25, 20]$ dBm (0.5 dB steps)
Load resistance R_{L} (multiband rectifier)	$\{0.057, 0.11, 0.18, 0.3, 0.47, 0.82, 1.5, 2.2, 3.3, 4.4, 5.5, 6.6, 7.8, 8.3, 9.3, 10, 15, 22, 39, 47, 56, 100, 120, 564\}$ kΩ
Load capacitance C_{L} (multiband rectifier)	15 pF
Load resistance R_{L} (simple rectifier)	287 Ω
Load capacitance C_{L} (simple rectifier)	115 pF
Baseband signal (sampling rate)	Multisine: $N \in \{1, 2, 4, 8, 16\}$ (40 MHz), pulsed RF (40 MHz), CSCG random vector (1 MHz), SC: M-PSK, 64-QAM (40 MHz), OFDM: QPSK, 64-QAM (1.92 MHz)
Tone spacing Δ_f (Multisine)	100 kHz
Duty cycle μ (pulsed RF)	$\{\frac{1}{16}, \frac{1}{10}, \frac{1}{8}, \frac{1}{4}, \frac{1}{2}\}$

by an oscilloscope, which is regulated by the same computer as before, through MATLAB. The computer registers the $V_{\text{out}}^{\text{dc}}$ data for each test baseband digital waveform and computes the receiver efficiency using (11). The hardware configuration for the test bed is showcased in Table II.

1) Calibration of P_{in}^{RF}: We measure (and later calibrate) $P_{\text{in}}^{\text{RF}}$, in our experiments, first by utilizing the real-time spectrum analyzer feature of the VST and later with the aid of an RF power meter. The measurements reveal that $P_{\text{in}}^{\text{RF}}$ deviates from its expected value owing to the inherent characteristics of the VST and RF PA. This issue is resolved as follows. The spectrum analyzer and RF power meter readings reveal that the VST used in this work could provide a linear output up to 0 dBm for a CW and that this linearity threshold declines with increasing the PAPR of the input signal. As a consequence, we opt for an RF PA to boost $P_{\text{out}}^{\text{RF}}$ to 20.5 dBm (so that $P_{\text{in}}^{\text{RF}} = 20$ dBm after cable attenuation). However, the PA too suffers from nonlinearity issues while transmitting high-PAPR signals. To overcome the nonlinearity problem, we introduce a lookup table-based power adjustment at the transmitter VST. For each $P_{\text{in}}^{\text{RF}}$ level, the calibrated lookup table entry is derived from the corresponding spectrum analyzer and RF power meter measurements. The input power to the RF PA is adjusted accordingly so that the true overall $P_{\text{in}}^{\text{RF}}$ is linear and exactly as required, for all the waveforms and at all input power levels.

2) Operational Parameters: Let us now present the operational parameters chosen for signals employed for the experiments. For the baseband multisine signal, we choose $f_n = (n - ((N+1)/2))\Delta_f$ so that the center frequency of the RF signal remains unchanged. Here, Δ_f is the frequency spacing between adjacent tones. In the case of pulsed RF waves, we vary the duty cycle μ to obtain a waveform with a PAPR similar to a multisine signal. For example, $\mu = 0.25$ yields a pulsed RF waveform with a PAPR of 8, similar to that of an $N = 4$ multisine. Next, we choose a circularly symmetric complex Gaussian (CSCG) random vector as the baseband signal for the Gaussian noise signal. Consequently, the resultant envelope signal would have a Rayleigh distribution. Furthermore, in the case of RF SWIPT signals, we select the symbol rate to be 1 MS/s. Overall, the operational parameters for the experiments are summarized in Table III.

3) Rectifier Circuits: One of the novel contributions of this research work is that the proposed rectifier model is invariant of the receiver architecture, viz., the matching network and the rectifier configuration. To validate this claim, we conduct the experiments for three different rectifier models: a simple rectifier circuit that was fabricated for this research work comprising a single Powercast PCC110 RF-to-dc converter [61] with an LC matching network matched to -5 dBm; an off-the-shelf multiband RF energy harvester Powercast P21XXCSR [53] with support for six frequency bands, each comprising two PCC110 chipsets with a T-matching network; and a voltage multiplier rectifier circuit based on the HSMS-282C diode, with an LC matching network matched to 0 dBm, simulated in Keysight Advanced Design System (ADS) software. The simple rectifier circuit developed on a PCB, along with its component values is presented in Fig. 4(a), whereas the multiband rectifier along with the T-matching network components is depicted in Fig. 4(b), while the schematic for the ADS simulation is presented in Fig. 4(c). In this way, we validate the proposed *waveform-to-EH* model for different diode types, as well as different matching network and rectifier configurations.

In Section V-B, we shall present the experimental results and compare them with simulation results based on the proposed rectifier model, in terms of the receiver efficiency. For the rectifier model, we determine the instantaneous efficiency $\eta(p)$ from the measurements for a CW, as described in Section III-A.

B. Results Validating the Proposed Rectifier Model

We measure the receiver efficiency for different RF WPT and RF SWIPT waveforms, for varying R_L, frequency band, and $P_{\text{in}}^{\text{RF}}$, and compare these outcomes with the predictions of the proposed rectifier model.

1) For Different Diode Types, Matching Networks, and Rectifier Configurations: In Fig. 5, we present the results for frequency band 2, for different RF WPT waveforms. It is evident from the three subfigures that the model predictions agree closely with the measurement outcomes for all three different RF EH circuits. Moreover, the measurements match very well even for multisine and pulsed RF waveforms, each with a different envelope signal distribution. Additionally, we also validate the model for a CSCG noise signal, where the envelope signal has a Rayleigh distribution, and the results in Fig. 5(a) and (b) confirm that the proposed model correctly predicts the receiver efficiency in this case as well. Overall, in each of the three rectifier models, we observe that a CW and a pulsed RF wave ($\mu = 0.1$) attain the highest η, which is about $37\%, 52\%, and 5\%$ for the fabricated rectifier,

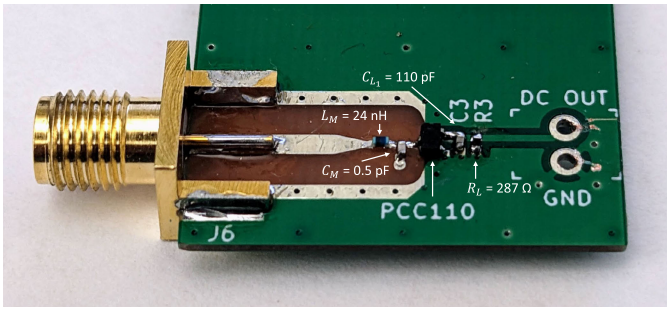

(a)

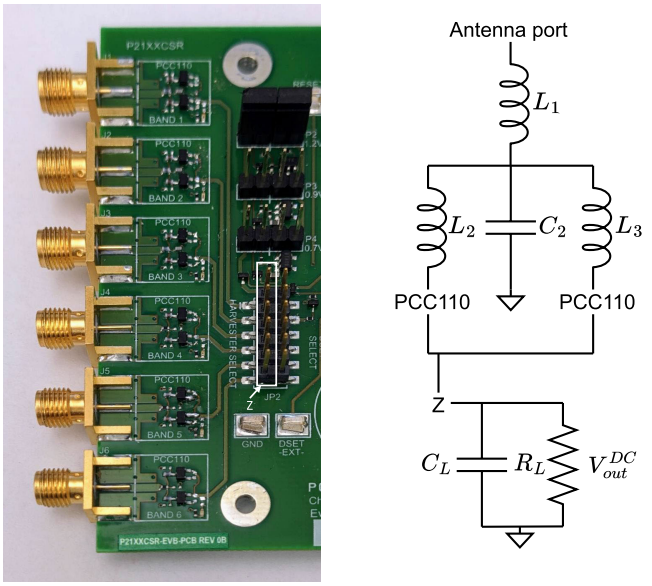

(b)

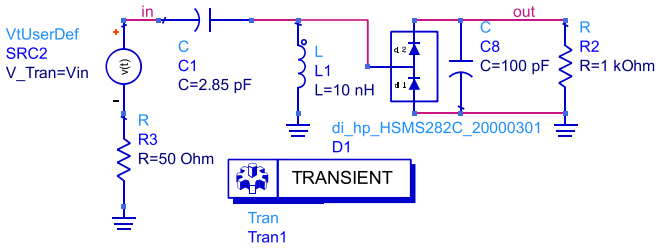

(c)

Fig. 4. RF energy harvesters employed in the experiments. (a) Rectifier circuit developed for this research work, comprising an LC matching network, a Powercast PCC110 RF-to-dc converter [61] with fixed load capacitance and resistance. The oscilloscope probe adds a series capacitance of 15 pF, resulting in a total $C_L = 115$ pF. (b) Off-the-shelf multiband RF energy harvester P21XXCSR [53], with each band comprising a T-matching network (as depicted separately) and two PCC110 RF-to-dc converters with fixed load capacitance and varying load resistance, which are connected to jumper pin Z [see Fig. 1(a)] corresponding to each band. The 15-pF capacitance of the oscilloscope probe acts as C_L. (c) Keysight ADS simulation of a rectifier circuit, comprising the SPICE model of an HSMS-282C series diode [62] connected in voltage multiplier configuration with a variable-load resistor and capacitor.

multiband rectifier, and simulated voltage-multiplier rectifier, respectively. Henceforth, we present the results only for the multiband rectifier.

2) For Multisine Waveforms and RF SWIPT Waveforms: Next, we evaluate the proposed model's predictions for the multisine waveforms (which have been claimed to be suitable for RF WPT in different research studies [7]) and we present the results for frequency band 2 of the multiband rectifier, in Fig. 6. It is apparent from Fig. 6 that the model predictions are accurate, within the measurement threshold, for all the multisines, from the low-PAPR two-multisine to the high-PAPR 16-multisine. We observe that in the low-power region, the high-PAPR multisines yield higher η: the higher the PAPR, the higher the instantaneous power level of the multisine signal which is essential to switch on the diodes at low $P_{\text{in}}^{\text{RF}}$ levels. Conversely, at higher $P_{\text{in}}^{\text{RF}}$ levels, the higher instantaneous power levels drive the diodes into saturation which may even result in reverse current, thus reducing the rate of increase of $V_{\text{out}}^{\text{dc}}$ with $P_{\text{in}}^{\text{RF}}$, and consequently beginning the reduction in η. This explains why the higher-PAPR signals reach the maximum efficiency at lower $P_{\text{in}}^{\text{RF}}$, compared to lower-PAPR signals and also why their receiver efficiency is significantly worse thereafter.

Moreover, we also observe that the model predictions are fairly precise across the entire range of $P_{\text{in}}^{\text{RF}}$, from the low power region to the saturation region. An important observation is that while the 16-multisine is the suitable waveform for lower $P_{\text{in}}^{\text{RF}}$, a CW still provides the maximum η, albeit at a much higher $P_{\text{in}}^{\text{RF}}$.

While the high-PAPR multisine waveforms are a popular choice for RF WPT, they are futile from a communication scenario. Hence, from a more practical point of view, we investigate the performance of our model for commonly used information signals appropriate for RF SWIPT, and the results are showcased in Fig. 7. It is clear from the measurements that the proposed model makes proper predictions for SWIPT signals as well across the entire $P_{\text{in}}^{\text{RF}}$ range, once their envelope signal distribution is known. Since an M-PSK signal essentially has the same envelope as a CW, the receiver efficiency for all M-PSK signals is the same. This corroborates our hypothesis of considering the instantaneous power of the envelope signal as the basis for our proposed model. Furthermore, similar to Fig. 6, we observe in Fig. 7 that the high-PAPR OFDM modulations are more suitable for lower $P_{\text{in}}^{\text{RF}}$ region than the low-PAPR SC modulations and worse at higher $P_{\text{in}}^{\text{RF}}$ region and vice versa. Even within the SC modulations, a 64-QAM signal with a slightly higher PAPR than M-PSK signals yields marginally better receiver efficiency than M-PSK modulations at lower $P_{\text{in}}^{\text{RF}}$ region.

It must be noted that the two measured OFDM modulations seem to yield different receiver efficiency since these are each a single finite-length realization. However, on average, the PAPR of an OFDM single is independent of the underlying modulation for high subcarrier points. Nonetheless, it is inconvenient to perform a large number of measurements to obtain an average result, and in such a case having a model that can precisely predict the performance is preferred, since averaging over simulations through the model is much more convenient. Accordingly, we present the averaged OFDM simulation result, based on the proposed model, in Fig. 7 and we observe that η is indeed independent of the baseband modulation.

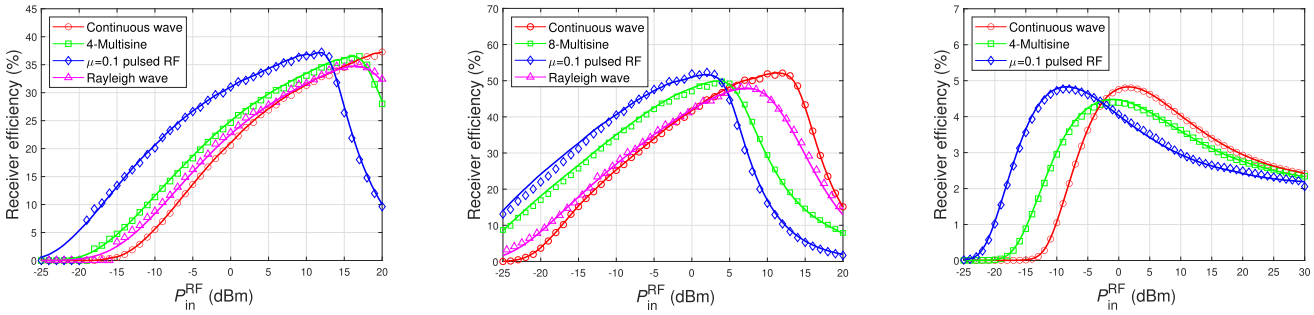

Fig. 5. Efficacy of the proposed rectifier model evaluated for three different rectifier circuits, while varying $P_{\text{in}}^{\text{RF}}$. For each rectifier, we compare the measured η for a CW, a multisine, a pulsed RF wave, and a noise signal with Rayleigh distributed amplitude. The measurement/simulation results are presented with markers, whereas the model prediction is displayed as a solid line. (a) Receiver efficiency of RF WPT waveforms for the fabricated RF energy harvester with $R_L = 287\ \Omega$ and $C_L = 115$ pF. (b) Receiver efficiency of RF WPT waveforms for an off-the-shelf multiband RF energy harvester with $R_L = 3.3$ kΩ and $C_L = 15$ pF in the frequency band 2. (c) Receiver efficiency of RF WPT waveforms for a voltage multiplier rectifier circuit simulated in ADS with $R_L = 1$ kΩ and $C_L = 100$ pF.

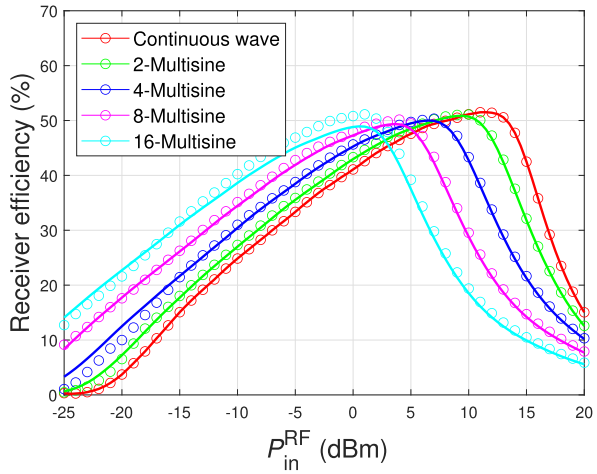

Fig. 6. Efficacy of the proposed rectifier model evaluated for multisine waveforms, while varying $P_{\text{in}}^{\text{RF}}$, with $R_L = 3.3$ kΩ, and $C_L = 15$ pF in the frequency band 2. The measurement results are presented with markers, whereas the model prediction is displayed as a solid line.

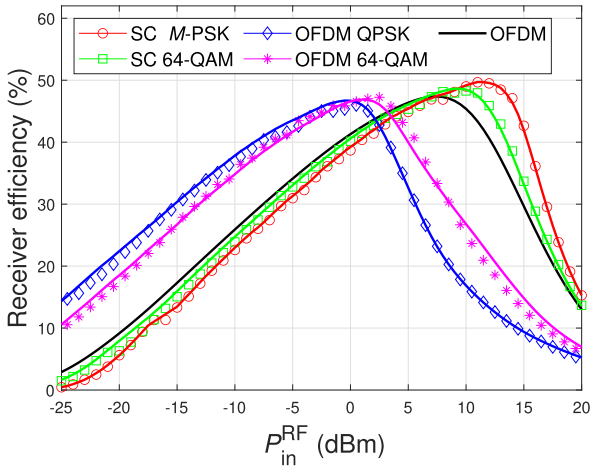

Fig. 7. Efficacy of the proposed rectifier model evaluated for RF SWIPT waveforms, while varying $P_{\text{in}}^{\text{RF}}$, with $R_L = 3.3$ kΩ and $C_L = 15$ pF in the frequency band 2. Here, OFDM QPSK and OFDM 64-QAM represent single high-PAPR realizations, while the others are general realizations of these waveforms. In general, the receiver efficiency for OFDM waveform is found to be independent of the baseband modulation. The measurement results are presented with markers and the model predictions with solid lines.

It must be noted that in the case of an RF WPT system, such as the one considered in our study, the received $P_{\text{in}}^{\text{RF}}$ varies between -30 and 20 dBm, since the best receiver sensitivity of even commercial RF EH receivers varies between -30 and -15 dBm [50], [53], [54]. In contrast, the receiver sensitivity of a typical communication node is much lower (≤ -80 dBm). Therefore, in the power range that is relevant to RF EH (even while employing the power-splitting scheme in RF SWIPT), the bit error rate for the communication receiver is practically zero [50]. We confirmed the same through wireless measurements for varying transmitter–receiver separation relevant to RF SWIPT in [54]. Hence, we omit to present the communication performance of the RF SWIPT waveforms in this study. Now, based on the observations of Figs. 5–7, we can deduce that, with the knowledge of $f_{\mathcal{P}}(p)$ and $\eta(p)$, the proposed model can rightly predict the receiver efficiency for any digital baseband waveform.

3) For Different Load Resistors: Next, we experimentally evaluated the receiver efficiency for the various load resistors described in Table III for different input waveforms (multisines and pulsed RF), PAPR and matching networks, and the results thereof along with the model predictions are depicted in the subplots of Fig. 8. These plots exhibit the efficacy of the proposed model in anticipating the receiver efficiency for a wide range of load resistance values. In Fig. 8(a), we present the receiver efficiency for different multisines (thus for varying PAPR) at certain $P_{\text{in}}^{\text{RF}}$. The $P_{\text{in}}^{\text{RF}}$ levels are chosen to present a clear, unconstricted figure. It is evident from Fig. 8(a) that the proposed model can correctly estimate the receiver efficiency for all the multisines and the entire range of R_L. The observations regarding the variation of receiver efficiency with R_L and multisine PAPR are consistent with those in [26]: At lower $P_{\text{in}}^{\text{RF}}$ values, a large R_L is needed to generate higher $V_{\text{out}}^{\text{dc}}$ and high-PAPR signals with their higher instantaneous values are more suitable. Contrarily at high $P_{\text{in}}^{\text{RF}}$ values, a low R_L is needed to avoid saturating the receiver and thus low-PAPR signals are more suitable.

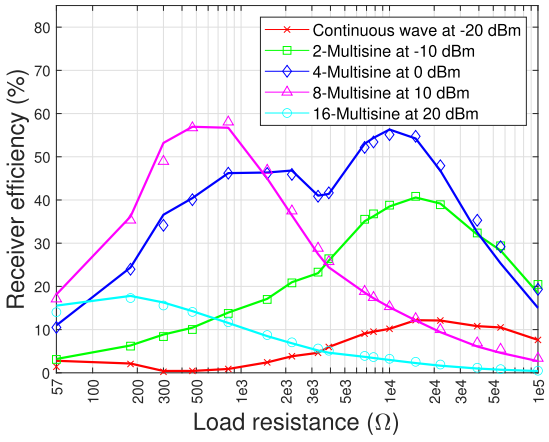

(a)

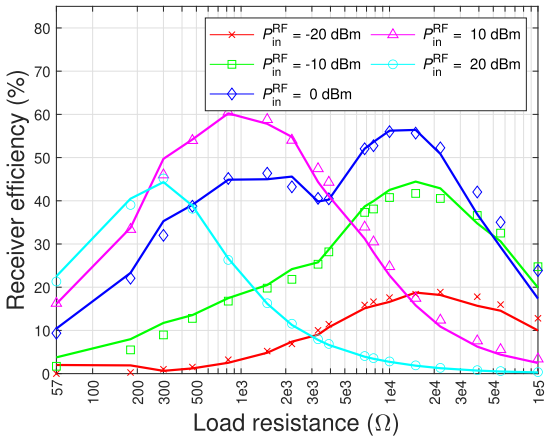

(b)

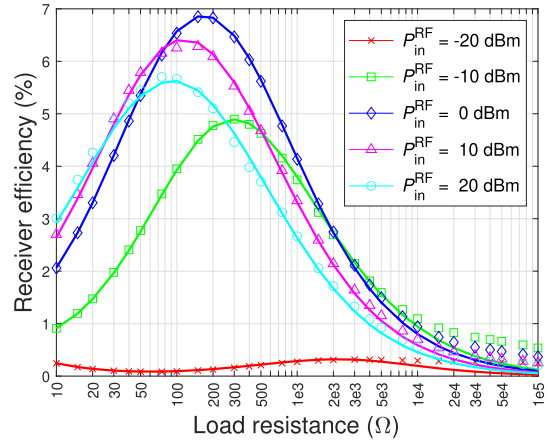

(c)

Fig. 8. Efficacy of the proposed rectifier model evaluated for different waveforms, PAPR, and matching networks, while varying R_L. The multiband harvester comprises a T-matching network, whereas the simulated rectifier circuit comprises an LC matching network. The measurement results are presented with markers and the model prediction is displayed as a solid line. (a) Receiver efficiency of different multisine waveforms for varying R_L, with $C_L = 15$ pF, at different $P_{\text{in}}^{\text{RF}}$ in the frequency band 2 of the multiband energy harvester. (b) Receiver efficiency of a pulsed RF waveform with 50% duty cycle for varying R_L, with $C_L = 15$ pF, at different $P_{\text{in}}^{\text{RF}}$ in the frequency band 2 of the multiband energy harvester. (c) Receiver efficiency of the eight-multisine waveform for varying R_L, for the voltage multiplier rectifier circuit with the LC matching network, simulated in ADS with $C_L = 100$ pF.

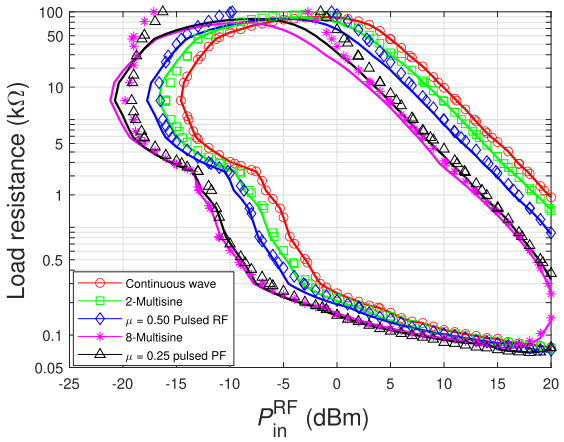

(a)

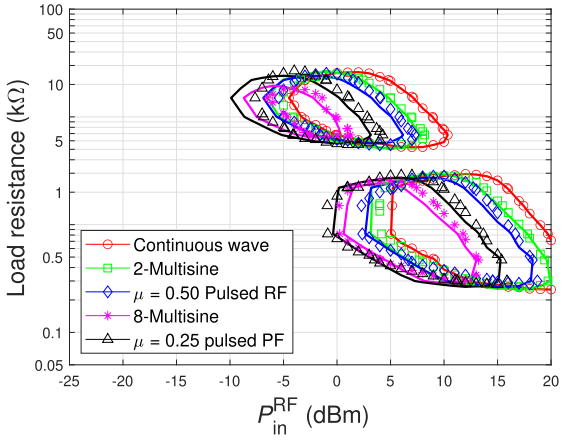

(b)

Fig. 9. Contour plots for average input RF power versus load resistance, showcasing the measurement results and model predictions of η for different RF WPT waveforms. The measurement results are presented with markers, whereas the model prediction is displayed as a solid line. (a) $\eta = 25\%$. (b) $\eta = 50\%$.

Furthermore, the receiver efficiency has been evaluated for the optimal pulsed RF waveform and the results are shown in Fig. 8(b). It is evident that the proposed model is capable of anticipating the receiver efficiency for pulsed RF waveform, within the measurement tolerance limits, for the entire range of load resistance R_L. The model outcomes are valid for low as well as high $P_{\text{in}}^{\text{RF}}$ regimes, including the saturation region. While the results shown in Fig. 8(a) and (b) correspond to the multiband RF energy harvester that comprises a T-matching network, the effectiveness of the proposed model in anticipating the receiver efficiency for an RF EH receiver with a different matching network is shown in Fig. 8(c). We resort to ADS simulations for this purpose and utilize the voltage multiplier rectifier circuit shown in Fig. 4(c) which comprises an LC matching network. We present the results for an eight-multisine signal in Fig. 8(c), wherein we observe that the efficacy of the proposed *waveform-to-EH* model in anticipating the receiver efficiency is invariant of the change in the matching network, for the entire range of $P_{\text{in}}^{\text{RF}}$ and all values of load resistance R_L.

Now, to further affirm the effectiveness of the proposed rectifier model for a wide range of $P_{\text{in}}^{\text{RF}}$ and R_L simultaneously, we present the contour plots of constant η versus $P_{\text{in}}^{\text{RF}}$ and R_L, similar to [63]. The contour plots for $\eta = 25\%$ and 50%

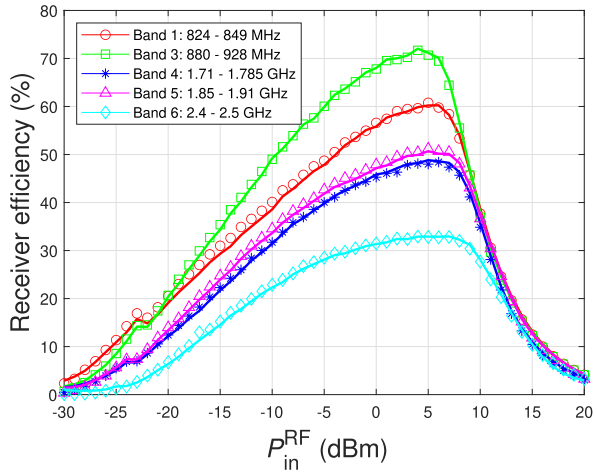

Fig. 10. Efficacy of the proposed rectifier model evaluated for different frequency bands of the multiband rectifier, for a $\mu = 0.25$ pulsed RF waveform, while varying $P_{\text{in}}^{\text{RF}}$, with $R_L = 3.3$ kΩ and $C_L = 15$ pF. The measurement results are presented with markers, whereas the model prediction is displayed as a solid line.

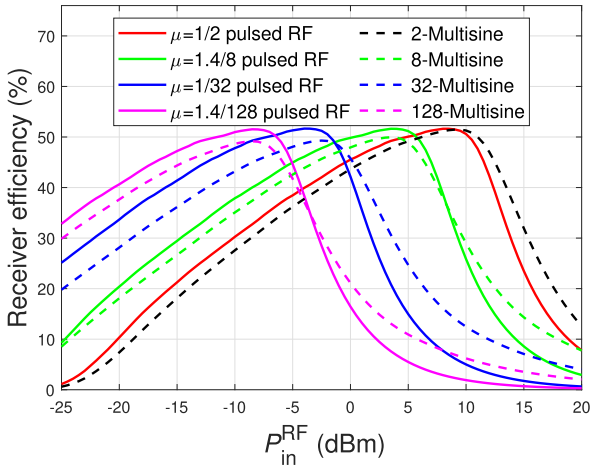

Fig. 11. Evaluating the receiver efficiency of multisine waveforms and pulsed RF waveforms to determine the waveform more suitable for RF WPT. The experimental results and model prediction corroborate the theoretical outcomes of the waveform optimization in Section IV.

are shown in Fig. 9(a) and (b), respectively, for multisines as well as pulsed RF waveforms with varying PAPR. The primary observation is that the model predictions match well with the measurements. The aberrations can be accredited to measurement inaccuracies owing to the resolution limitations of the oscilloscope at high R_L for high PAPR signals, where the instantaneous voltage is very high. Furthermore, although the two-multisine and $\mu = 0.5$ pulsed RF waveform have the same PAPR, we observe that the pulsed RF waveform achieves the same η at a lower $P_{\text{in}}^{\text{RF}}$. Even more remarkable is the observation that $\mu = 0.25$ pulsed RF waveform has a contour plot similar to eight-multisine, even though the latter has twice the PAPR. We shall explore this in further detail in Section V-C1.

4) For Different Frequency Bands: Thus far, we presented the results only for the frequency band 2 of the multiband rectifier. We now confirm whether the proposed model can make correct predictions of η for other the frequency bands described in Table III. In Fig. 10, we present the measurement and modeling results for different RF bands for a pulsed RF wave with 25% duty cycle. Although the multiband harvester comprises the same RF-to-dc rectifier chips in all the frequency bands [53], the preceding T-matching network components vary in each frequency band. It is evident in Fig. 10 that the proposed model can correctly predict η for all the frequency bands of the off-the-shelf multiband rectifier. This reaffirms that the efficacy of the proposed model is invariant of the underlying matching network. Among all the bands, frequency band 3 of the multiband rectifier yields the highest η of about 72%. Meanwhile, the unlicensed band 6 has a maximum η of about 33%.

C. Results Validating the Waveform Optimization

The waveform optimization problem based on the proposed novel rectifier model was discussed in Section IV, wherein we concluded that a pulsed RF waveform is an optimal transmit waveform. In this section, we focus specifically on the η performance of a pulsed RF waveform in RF WPT. Here as well, we present the results for the frequency band 2 of the multiband rectifier, with the operational parameters being the same as before.

1) Pulsed RF Versus Multisines: To verify the theoretical result of Section IV, we experimentally determined the receiver efficiency η of a pulsed RF wave for varying duty cycle μ and compared these with the measurements with N-multisines. We opt for a multisine, with the same $P_{\text{in}}^{\text{RF}}$, as the reference waveform since multisines are recommended as optimal waveforms for RF WPT [7]. An N-multisine signal will have the same PAPR as $\mu = (1/N)$-pulsed RF signal and is expected to yield similar η performance. However, our model reveals (and the measurements confirm) that this is not the case. To have an unconstricted plot, we choose to showcase the plots obtained from the proposed rectifier model in Fig. 11. Before the onset of saturation, a $\mu = (1/N)$-pulsed RF signal yields higher efficiency than an N-multisine due to the former having peak instantaneous power for a longer duration. However, once the diodes enter the saturation region, so-clipped multisine signals have a longer duration of peak instantaneous power, thus yielding higher η. Additionally, it also results in a $\mu = (1/N)$-pulsed RF signal reaching peak η at a lower $P_{\text{in}}^{\text{RF}}$ than an N-multisine. These effects can be observed for the cases of $N = 2$ and 32 in Fig. 11. Consequently, we need a pulsed RF with a longer duty cycle $\mu = (1/M)(M < N)$ for that signal to have a peak η at the same $P_{\text{in}}^{\text{RF}}$ as an N-multisine, as seen in the other two cases in Fig. 11. Overall, it is evident that a pulsed RF signal outperforms an N-multisine signal at any given $P_{\text{in}}^{\text{RF}}$ that is viable in RF WPT.

2) Receiver Efficiency η Variation With Duty Cycle μ: Our theoretical exercise in Section IV led us to conclude that a pulsed RF waveform with duty cycle μ is optimal for RF WPT, with the impulse signal being ideal, and the choice of μ is influenced by the available bandwidth and permitted signal duration T. In Fig. 12, we present the variation of η for varying μ. We observe that the proposed model can

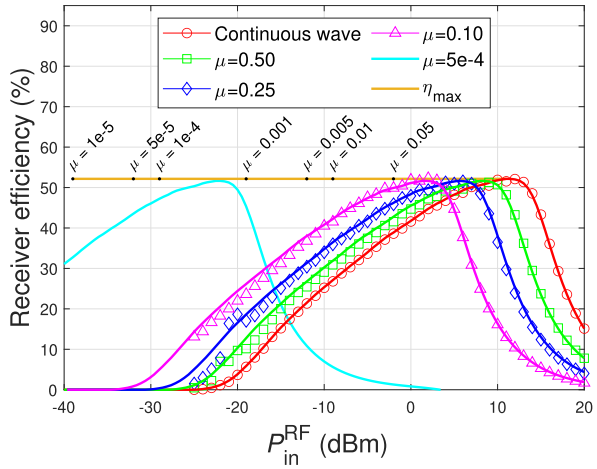

Fig. 12. Variation of receiver efficiency with varying μ and $P_{\text{in}}^{\text{RF}}$ for a pulsed RF waveform, determined by the proposed rectifier model and verified with measurements, with $R_L = 3.3$ kΩ and $C_L = 15$ pF in the frequency band 2. The model allows us to ascertain the optimal μ that attains maximum η at each $P_{\text{in}}^{\text{RF}}$. The measurement results are presented with markers, whereas the model prediction is displayed as a solid line.

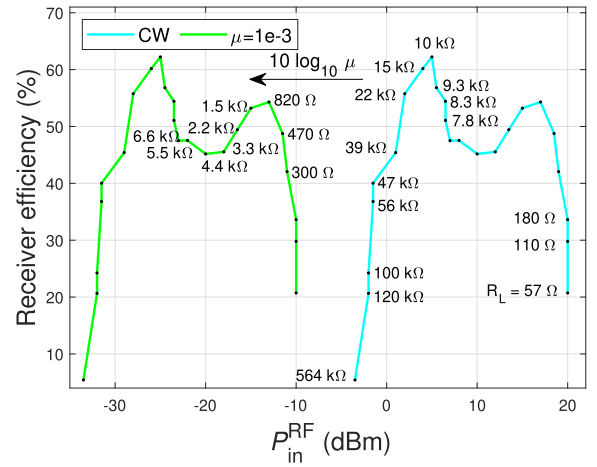

Fig. 13. Variation of receiver efficiency with duty cycle and load resistance for a pulsed RF wave. We measure the receiver efficiency with a CW for different resistors and the model allows us to determine the receiver efficiency at any duty cycle μ, which shifts the curve to the left by $10\log_{10}(\mu)$. The maximum attainable efficiency is ≈62% for $R_L = 10$ kΩ.

correctly predict the impact of varying μ. The mismatch at lower $P_{\text{in}}^{\text{RF}}$ can be attributed to measurement inaccuracies of the oscilloscope and the high noise floor of the PA. For a given $P_{\text{in}}^{\text{RF}}$, reducing μ by $(1/N)$ increases the peak instantaneous power of the RF waveform by N, when compared to a CW ($\mu = 1$). The increased peak instantaneous power yields higher η at lower $P_{\text{in}}^{\text{RF}}$ similar to multisines, albeit better. In fact, reducing μ by N shifts the η plot for a CW in Fig. 12 by $-10\log_{10}\mu$ dB. The proposed model allows us to determine η for very low values of μ, which is not possible to evaluate experimentally due to the limited dynamic range of the PA. In Fig. 12, we reduce μ progressively and track the maximum receiver efficiency $\eta_{\max}$, which is the peak efficiency attainable at each $P_{\text{in}}^{\text{RF}}$, while employing the frequency band 2 of the multiband rectifier with $R_L = 3300$ Ω.

3) Maximum Receiver Efficiency $\eta_{\max}$ Versus Load Resistance and Duty Cycle: Furthermore, we examine how $\eta_{\max}$ varies as we vary both the load resistance R_L and μ, and the results are illustrated in Fig. 13. Apparently, for a given μ, the smallest $R_L = 57$ Ω yields $\eta_{\max} \approx 21\%$, while the highest $R_L = 10$ kΩ yields $\eta_{\max} \approx 62\%$. The smaller load resistors are suitable at higher $P_{\text{in}}^{\text{RF}}$, while the larger R_L are suited for lower $P_{\text{in}}^{\text{RF}}$, as explained in Section V-B3. In some cases, multiple load resistors provide the same $\eta_{\max}$ but at different $P_{\text{in}}^{\text{RF}}$: for example, $R_L = 470, 2200$, and 7800 Ω each yield $\eta_{\max} = 50\%$. In such cases, R_L providing the desired $V_{\text{out}}^{\text{dc}}$ is suitable. Once again, in general, the desired $\eta_{\max}$ can be attained at a lower $P_{\text{in}}^{\text{RF}}$ by reducing the duty cycle μ.

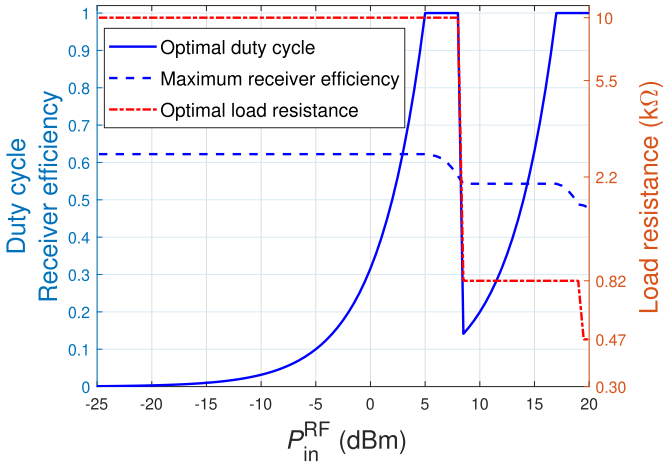

Fig. 14. Maximum attainable receiver efficiency at each $P_{\text{in}}^{\text{RF}}$ across all the load resistors, and the corresponding duty cycle for the frequency band 2 of the multiband rectifier. The 10-kΩ load resistor is optimal for a major portion of $P_{\text{in}}^{\text{RF}}$, notably in the low-power regime.

D. Maximum Receiver Efficiency at Each P_{in}^{RF}

Once we figure out the maximum receiver efficiency $\eta_{\max}$ attainable for each load resistance R_L, the next apparent goal is to determine the $\eta_{\max}$ achievable for each average input RF power level $P_{\text{in}}^{\text{RF}}$. Based on the measurements of receiver efficiency for a CW for different R_L, and the subsequent model predictions for varying μ, we present the maximum attainable η for each $P_{\text{in}}^{\text{RF}}$ in Fig. 14. For the multiband rectifier in use, we observe in Fig. 13 that $R_L = 10$ kΩ yields the maximum efficiency for a CW, among all R_L, at $P_{\text{in}}^{\text{RF}} = 5$ dBm. It is possible to attain the same maximum efficiency for any $P_{\text{in}}^{\text{RF}} < 5$ dBm by reducing μ. The optimal duty cycle at each $P_{\text{in}}^{\text{RF}}$ is also shown in Fig. 14. Moreover, the optimal R_L which yields the maximum η at each $P_{\text{in}}^{\text{RF}}$ is also depicted in Fig. 14.

VI. Conclusion

This article studies the receiver efficiency of an RF WPT system and presents a novel rectifier model that characterizes the average harvested dc power in terms of the baseband signal of the input RF waveform. The proposed parametric model is independent of the underlying matching network or the rectifier and thus is applicable and accurate for any EH receiver for which model parameters are estimated from measurements or simulations. The rectifier model allows us to design the optimal transmit baseband signal for RF WPT such that

the average harvested dc power is maximized. Furthermore, a test bed to experimentally evaluate the receiver efficiency for any digital waveform is introduced. The experimental results and simulations, both validate the predictions of the proposed rectifier model for popular RF WPT and RF SWIPT waveforms as well as validate the theoretical result of pulsed RF waveforms being superior to multisine waveforms for RF WPT and suitable for RF SWIPT. The receiver efficiency of SWIPT with PSK, QAM, and OFDM is also evaluated through the model and verified experimentally.

REFERENCES

[1] B. Clerckx, A. Costanzo, A. Georgiadis, and N. B. Carvalho, "Toward 1G mobile power networks: RF, signal, and system designs to make smart objects autonomous," *IEEE Microw. Mag.*, vol. 19, no. 6, pp. 69–82, Sep. 2018.

[2] T. D. Ponnimbaduge Perera, D. N. K. Jayakody, S. K. Sharma, S. Chatzinotas, and J. Li, "Simultaneous wireless information and power transfer (SWIPT): Recent advances and future challenges," *IEEE Commun. Surveys Tuts.*, vol. 20, no. 1, pp. 264–302, 1st Quart., 2018.

[3] M. Rayes, G. Nagib, and W. Abdelaal, "A review on wireless power transfer," *Int. J. Eng. Trends Technol.*, vol. 40, no. 5, pp. 272–280, Oct. 2016.

[4] Wireless Power Consortium. *Magnetic Resonance and Magnetic Induction*. Accessed: Apr. 6, 2023. [Online]. Available: https://www.wirelesspowerconsortium.com/data/downloadables/1/2/4/6/magnetic-resonance-or-magnetic-induction.pdf

[5] Digikey. *Inductive Versus Resonant Wireless Charging: Truce May Be Designer's Best Choice*. Accessed: Apr. 6, 2023. [Online]. Available: https://www.digikey.fi/en/articles/inductive-versus-resonant-wireless-charging

[6] Ansys. *Wireless Charging Technologies: Magnetic Resonance vs. Magnetic Induction vs. RF Harvesting*. Accessed: Apr. 6, 2023. [Online]. Available: https://www.ansys.com/blog/ces-wireless-charging-magnetic-resonance-induction-RF-harvesting/

[7] B. Clerckx, R. Zhang, R. Schober, D. W. K. Ng, D. I. Kim, and H. V. Poor, "Fundamentals of wireless information and power transfer: From RF energy harvester models to signal and system designs," *IEEE J. Sel. Areas Commun.*, vol. 37, no. 1, pp. 4–33, Jan. 2019.

[8] Y. Chen, K. T. Sabnis, and R. A. Abd-Alhameed, "New formula for conversion efficiency of RF EH and its wireless applications," *IEEE Trans. Veh. Technol.*, vol. 65, no. 11, pp. 9410–9414, Nov. 2016.

[9] N. Ayir, T. Riihonen, M. Allén, and M. F. T. Fierro, "Waveforms and end-to-end efficiency in RF wireless power transfer using digital radio transmitter," *IEEE Trans. Microw. Theory Techn.*, vol. 69, no. 3, pp. 1917–1931, Mar. 2021.

[10] J. Hu, K. Yang, G. Wen, and L. Hanzo, "Integrated data and energy communication network: A comprehensive survey," *IEEE Commun. Surveys Tuts.*, vol. 20, no. 4, pp. 3169–3219, 4th Quart., 2018.

[11] Y. Alsaba, S. K. A. Rahim, and C. Y. Leow, "Beamforming in wireless energy harvesting communications systems: A survey," *IEEE Commun. Surveys Tuts.*, vol. 20, no. 2, pp. 1329–1360, 2nd Quart., 2018.

[12] C. R. Valenta and G. D. Durgin, "Harvesting wireless power: Survey of energy-harvester conversion efficiency in far-field, wireless power transfer systems," *IEEE Microw. Mag.*, vol. 15, no. 4, pp. 108–120, Jun. 2014.

[13] X. Lu, P. Wang, D. Niyato, D. I. Kim, and Z. Han, "Wireless networks with RF energy harvesting: A contemporary survey," *IEEE Commun. Surveys Tuts.*, vol. 17, no. 2, pp. 757–789, 2nd Quart., 2015.

[14] A. Boaventura, D. Belo, R. Fernandes, A. Collado, A. Georgiadis, and N. B. Carvalho, "Boosting the efficiency: Unconventional waveform design for efficient wireless power transfer," *IEEE Microw. Mag.*, vol. 16, no. 3, pp. 87–96, Apr. 2015.

[15] N. Ayir, M. F. T. Fierro, T. Riihonen, and M. Allén, "Experimenting waveforms and efficiency in RF power transfer," in *IEEE MTT-S Int. Microw. Symp. Dig.*, Jun. 2019, pp. 1140–1143.

[16] Md. A. Ullah, R. Keshavarz, M. Abolhasan, J. Lipman, K. P. Esselle, and N. Shariati, "A review on antenna technologies for ambient RF energy harvesting and wireless power transfer: Designs, challenges and applications," *IEEE Access*, vol. 10, pp. 17231–17267, 2022.

[17] H. Rahmani and A. Babakhani, "A wireless power receiver with an on-chip antenna for millimeter-size biomedical implants in 180 nm SOI CMOS," in *IEEE MTT-S Int. Microw. Symp. Dig.*, Jun. 2017, pp. 300–303.

[18] Y. Sun, B. Greet, D. Burkland, M. John, M. Razavi, and A. Babakhani, "Wirelessly powered implantable pacemaker with on-chip antenna," in *IEEE MTT-S Int. Microw. Symp. Dig.*, Jun. 2017, pp. 1242–1244.

[19] J. F. Kuhling, M. Feenaghty, and R. Dahle, "A wideband cascaded skew planar wheel antenna for RF energy harvesting," in *Proc. IEEE Wireless Power Transf. Conf. (WPTC)*, Jun. 2018, pp. 1–4.

[20] M. M. Fakharian, "A wideband Rectenna using high gain fractal planar monopole antenna array for RF energy scavenging," *Int. J. Antennas Propag.*, vol. 2020, pp. 1–10, Jun. 2020.

[21] K. Saito, E. Nishiyama, and I. Toyoda, "A 2.45- and 5.8-GHz dual-band stacked differential Rectenna with high conversion efficiency in low power density environment," *IEEE Open J. Antennas Propag.*, vol. 3, pp. 627–636, 2022.

[22] J. Kim, B. Clerckx, and P. D. Mitcheson, "Prototyping and experimentation of a closed-loop wireless power transmission with channel acquisition and waveform optimization," in *Proc. IEEE Wireless Power Transf. Conf. (WPTC)*, May 2017, pp. 1–4.

[23] A. Georgiadis, G. V. Andia, and A. Collado, "Rectenna design and optimization using reciprocity theory and harmonic balance analysis for electromagnetic (EM) energy harvesting," *IEEE Antennas Wireless Propag. Lett.*, vol. 9, pp. 444–446, 2010.

[24] P. N. Duy, N. Ha-Van, and C. Seo, "A design of 5.8 GHz rectenna array for wireless energy harvesting applications," in *Proc. IEEE Wireless Power Transf. Conf. (WPTC)*, Nov. 2020, pp. 87–90.

[25] N. Ayir, M. Heino, and T. Riihonen, "Impact of input impedance mismatch on the receiver efficiency of RF wireless power transfer," in *Proc. Wireless Power Week (WPW)*, Jul. 2022, pp. 412–416.

[26] N. Ayir and T. Riihonen, "Joint impact of input power, PAPR, and load resistance on the receiver efficiency of multisine waveforms in RF energy harvesting," in *Proc. IEEE Wireless Power Transf. Conf. (WPTC)*, Jun. 2021, pp. 1–4.

[27] E. Boshkovska, D. W. K. Ng, N. Zlatanov, and R. Schober, "Practical non-linear energy harvesting model and resource allocation for SWIPT systems," *IEEE Commun. Lett.*, vol. 19, no. 12, pp. 2082–2085, Dec. 2015.

[28] M. Babaei, L. Durak-Ata, and Ü. Aygölü, "New practical nonlinear energy-harvesting models for wireless-powered communications," *Wireless Commun. Mobile Comput.*, vol. 2022, pp. 1–19, Jun. 2022.

[29] X. Xu, A. Özçelikkale, T. McKelvey, and M. Viberg, "Simultaneous information and power transfer under a non-linear RF energy harvesting model," in *Proc. IEEE Int. Conf. Commun. Workshops (ICC Workshops)*, May 2017, pp. 179–184.

[30] E. Boshkovska, D. W. K. Ng, N. Zlatanov, A. Koelpin, and R. Schober, "Robust resource allocation for MIMO wireless powered communication networks based on a non-linear EH model," *IEEE Trans. Commun.*, vol. 65, no. 5, pp. 1984–1999, May 2017.

[31] R. Jiang, K. Xiong, P. Fan, Y. Zhang, and Z. Zhong, "Optimal design of SWIPT systems with multiple heterogeneous users under non-linear energy harvesting model," *IEEE Access*, vol. 5, pp. 11479–11489, 2017.

[32] A. J. S. Boaventura and N. B. Carvalho, "Maximizing DC power in energy harvesting circuits using multisine excitation," in *IEEE MTT-S Int. Microw. Symp. Dig.*, Jun. 2011, pp. 1–4.

[33] B. Clerckx and E. Bayguzina, "Waveform design for wireless power transfer," *IEEE Trans. Signal Process.*, vol. 64, no. 23, pp. 6313–6328, Dec. 2016.

[34] S. Abeywickrama, R. Zhang, and C. Yuen, "Refined nonlinear Rectenna modeling and optimal waveform design for multi-user multi-antenna wireless power transfer," *IEEE J. Sel. Topics Signal Process.*, vol. 15, no. 5, pp. 1198–1210, Aug. 2021.

[35] M. R. V. Moghadam, Y. Zeng, and R. Zhang, "Waveform optimization for radio-frequency wireless power transfer: (Invited paper)," in *Proc. IEEE 18th Int. Workshop Signal Process. Adv. Wireless Commun. (SPAWC)*, Jul. 2017, pp. 1–6.

[36] Y. Huang and B. Clerckx, "Waveform design for wireless power transfer with limited feedback," *IEEE Trans. Wireless Commun.*, vol. 17, no. 1, pp. 415–429, Jan. 2018.

[37] L. Cantos, G. Sacarelo, Y. Jeong, and Y. H. Kim, "Performance of a waveform design for wireless power transfer with imperfect channel state information," in *Proc. Int. Conf. Inf. Commun. Technol. Converg. (ICTC)*, Oct. 2017, pp. 1293–1295.

[38] E. Boshkovska, A. Koelpin, D. W. K. Ng, N. Zlatanov, and R. Schober, "Robust beamforming for SWIPT systems with non-linear energy harvesting model," in *Proc. IEEE 17th Int. Workshop Signal Process. Adv. Wireless Commun. (SPAWC)*, Jul. 2016, pp. 1–5.

[39] H. Sun, F. Zhou, and Z. Zhang, "Robust beamforming design in a NOMA cognitive radio network relying on SWIPT," in *Proc. IEEE Int. Conf. Commun. (ICC)*, May 2018, pp. 1–6.

[40] B. Clerckx and J. Kim, "On the beneficial roles of fading and transmit diversity in wireless power transfer with nonlinear energy harvesting," *IEEE Trans. Wireless Commun.*, vol. 17, no. 11, pp. 7731–7743, Nov. 2018.

[41] Y. Zeng, B. Clerckx, and R. Zhang, "Communications and signals design for wireless power transmission," *IEEE Trans. Commun.*, vol. 65, no. 5, pp. 2264–2290, May 2017.

[42] J. Kim, B. Clerckx, and P. D. Mitcheson, "Signal and system design for wireless power transfer : Prototype, experiment and validation," *IEEE Trans. Wireless Commun.*, p. 1, 2020.

[43] E. Davut, O. Kazanci, A. Caglar, D. Altinel, M. B. Yelten, and G. K. Kurt, "A test-bed based guideline for multi-source energy harvesting," in *Proc. 10th Int. Conf. Elect. Electron. Eng.*, Nov. 2017, pp. 1267–1271.

[44] M. Cansiz, D. Altinel, and G. K. Kurt, "Effects of different modulation techniques on charging time in RF energy-harvesting system," *IEEE Trans. Instrum. Meas.*, vol. 69, no. 9, pp. 6904–6911, Sep. 2020.

[45] S. Nikoletseas, T. Raptis, A. Souroulagkas, and D. Tsolovos, "Wireless power transfer protocols in sensor networks: Experiments and simulations," *J. Sensor Actuator Netw.*, vol. 6, no. 2, p. 4, Apr. 2017.

[46] K. Li, C. Yuen, and S. Jha, "Poster: Fair scheduling for energy harvesting WSN in smart city," in *Proc. 13th ACM Conf. Embedded Networked Sensor Syst.*, Nov. 2015, pp. 419–420.

[47] H. Dai, X. Wang, A. X. Liu, F. Zhang, Y. Zhao, and G. Chen, "Omnidirectional chargability with directional antennas," in *Proc. IEEE 24th Int. Conf. Netw. Protocols (ICNP)*, Nov. 2016, pp. 1–10.

[48] P. S. Yedavalli, T. Riihonen, X. Wang, and J. M. Rabaey, "Far-field RF wireless power transfer with blind adaptive beamforming for Internet of Things devices," *IEEE Access*, vol. 5, pp. 1743–1752, 2017.

[49] X. Fan et al., "Energy-ball: Wireless power transfer for batteryless Internet of Things through distributed beamforming," *Proc. ACM Interact., Mobile, Wearable Ubiquitous Technol.*, vol. 2, no. 2, pp. 1–22, Jul. 2018.

[50] J. Kim, B. Clerckx, and P. D. Mitcheson, "Experimental analysis of harvested energy and throughput trade-off in a realistic SWIPT system," in *Proc. IEEE Wireless Power Transf. Conf. (WPTC)*, Jun. 2019, pp. 1–5.

[51] S. Claessens, N. Pan, D. Schreurs, and S. Pollin, "Multitone FSK modulation for SWIPT," *IEEE Trans. Microw. Theory Techn.*, vol. 67, no. 5, pp. 1665–1674, May 2019.

[52] B. Clerckx, J. Kim, K. W. Choi, and D. I. Kim, "Foundations of wireless information and power transfer: Theory, prototypes, and experiments," *Proc. IEEE*, vol. 110, no. 1, pp. 8–30, Jan. 2022.

[53] Powercast. *P211XXCSR-EVB Datasheet*. Accessed: Apr. 6, 2023. [Online]. Available: https://www.powercastco.com/documentation/p21xxcsr-evb-datasheet/

[54] N. Ayir and T. Riihonen, "Efficiency–throughput trade-off of pulsed RF waveforms in simultaneous wireless information and power transfer," in *Proc. Wireless Power Technol. Conf. Expo (WPTCE)*, Jun. 2023, pp. 1–15.

[55] R. Zhang and C. K. Ho, "MIMO broadcasting for simultaneous wireless information and power transfer," *IEEE Trans. Wireless Commun.*, vol. 12, no. 5, pp. 1989–2001, May 2013.

[56] R. Burden and J. Faires, *Numerical Analysis*. Pacific Grove, CA, USA: Brooks Cole, 2004.

[57] Mini-Circuits. *Mini-Circuits ZHL-4240+ Datasheet*. Accessed: Apr. 6, 2023. [Online]. Available: https://www.minicircuits.com/pdfs/ZHL-4240+.pdf

[58] Apex Waves. *NI PXIe-5645R Specifications*. Accessed: Apr. 6, 2023. [Online]. Available: https://www.apexwaves.com/pdf/manuals/PXIe-5665/pxie-5645r-specifications.pdf

[59] Keysight. *Keysight MSOX4104A Datasheet*. Accessed: Apr. 6, 2023. [Online]. Available: https://www.keysight.com/us/en/assets/7018-03631/data-sheets/5991-1103.pdf

[60] Farnell. *R&S NRP-Z11 Datasheet*. Accessed: Apr. 6, 2023. [Online]. Available: https://www.farnell.com/datasheets/2176138.pdf

[61] Powercast. *PCC110 Chipset Datasheet*. Accessed: Apr. 6, 2023. [Online]. Available: https://www.powercastco.com/documentation/pcc110-pcc210-chipset-overview/

[62] Datasheetspdf. *HSMS-282X Datasheet*. Accessed: Apr. 6, 2023. [Online]. Available: https://datasheetspdf.com/pdf-file/963462/AVAGO/HSMS-282C/1

[63] F. Bolos, J. Blanco, A. Collado, and A. Georgiadis, "RF energy harvesting from multi-tone and digitally modulated signals," *IEEE Trans. Microw. Theory Techn.*, vol. 64, no. 6, pp. 1918–1927, Jun. 2016.

Nachiket Ayir (Member, IEEE) received the M.Sc. degree in electronics and communications engineering from the International Institute of Information Technology, Hyderabad, India, in May 2018.

He is currently with the Faculty of Information Technology and Communication Sciences, Tampere University, Tampere, Finland, as a Doctoral Researcher. His current research interests include wireless energy harvesting, optimization techniques, software-defined radios, and simultaneous wireless information and power transfer.

Taneli Riihonen (Senior Member, IEEE) received the D.Sc. degree (Hons.) in electrical engineering from Aalto University, Espoo, Finland, in August 2014.

He held various research positions at the School of Electrical Engineering, Aalto University, from September 2005 to December 2017. He was a Visiting Associate Research Scientist and an Adjunct Assistant Professor with Columbia University, New York, NY, USA, from November 2014 to December 2015. He is currently an Associate Professor (Tenure Track) with the Faculty of Information Technology and Communication Sciences, Tampere University, Tampere, Finland. His research interests include physical-layer OFDM(A), multiantennas, relaying, and full-duplex wireless techniques with current interest in the evolution of 6G systems.

Mr. Riihonen received the Finnish Technical Sector's Award for the best doctoral dissertation of the year and the EURASIP Best Ph.D. Thesis Award 2017. He has been nominated 12 times as an Exemplary/Top Reviewer/Editor of various IEEE journals and is serving as an Editor for IEEE TRANSACTIONS ON WIRELESS COMMUNICATIONS. He has previously served as an Editor for IEEE COMMUNICATIONS LETTERS and IEEE WIRELESS COMMUNICATIONS LETTERS.

Mikko Heino (Member, IEEE) received the D.Sc. degree in radio engineering from Aalto University, Espoo, Finland, in 2020.

He is currently a Post-Doctoral Research Fellow with the Unit of Electrical Engineering, Tampere University, Tampere, Finland. His research interests include antenna isolation improvement methods, joint communication and sensing, in-band full-duplex antenna design, and the user effect of millimeter-wave handset antennas.